MDPI

Review

Crack Formation Mechanisms and Control Methods of Laser Cladding Coatings: A Review

Mingke Li, Kepeng Huang and Xuemei Yi *

College of Mechanical and Electronic Engineering, Northwest Agriculture and Forestry University, Xianyang 712100, China; limingke@nwafu.edu.cn (M.L.); kepeng_huang@nwafu.edu.cn (K.H.)
* Correspondence: xuemei_yi@nwsuaf.edu.cn; Tel.: +86-29-8709-2391

Abstract: Laser cladding, a novel surface treatment technology, utilizes a high-energy laser beam to melt diverse alloy compositions and form a specialized alloy-cladding layer on the surface of the substrate to enhance its property. However, it can generate substantial residual stresses during the rapid cooling and heating stages, due to inadequate selection of cladding process parameters and disparities in thermophysical properties between the clad layer and substrate material, leading to the formation of various types of cracks. These cracks can significantly impact the quality and performance of the coating. This paper presents a comprehensive review of crack types and their causes in laser cladding coatings, and identifies that three primary sources of residual stresses, thermal stress, organizational stress, and restraint stress, are the fundamental causes of crack formation. The study proposes several strategies to control coating cracks, including optimizing the coating layer material, refining the coating process parameters, incorporating heat treatment, applying auxiliary fields, and utilizing numerical simulations to predict crack initiation and propagation. Additionally, the paper summarizes crack control methods for emerging structural materials and novel preparation processes. Lastly, the paper analyzes the prospects, technical approaches, and key research directions for effectively controlling cracks in laser cladding coatings.

Keywords: laser cladding coating; cracks; residual stress; causes; control methods

1. Introduction

Laser cladding (LC) is an advanced surface modification technology that utilizes a high-energy laser beam to melt the clad material, forming a strong metallurgical bond with the substrate material [1]. This technology offers numerous advantages, including high bond strength, minimal heat-affected zone, low thermal deformation, and low dilution rate [2–4]. It has found extensive applications in aerospace, automotive, and chemical industries, among others [5–7]. The LC system usually consists of a KUKA robot or robot arm, LC head, powder feeder, protective gas, water cooling system, and workbench [8] (Figure 1).

Despite the excellent performance of laser melting coatings, the rapid melting and solidification process can give rise to defects such as cracks, porosity, and inclusions within the coating. Among these defects, cracks are the most common internal issue in the laser cladding process [9,10]. Microscopic cracks within the coating can propagate into macroscopic cracks under working loads, significantly compromising the coating's quality [11]. Consequently, current research focuses on suppressing or eliminating internal cracks in laser cladding coatings, which presents a challenging and active area of study [12,13].

In recent years, scholars have conducted extensive experimental research on the causes and control methods of cracks in laser cladding coatings. Zhang et al. [14] and Galy et al. [15] reviewed the solidification theory of the selective laser melting (SLM) process and the formation mechanisms of the hole and crack defects. Quazi et al. [16] discussed the influence of rare earth additives on the crack sensitivity of coatings. Similarly, Wang et al. [17] and Hu et al. [18] suggested improvement strategies, including optimizing

process parameters and employing preheating treatments, to mitigate coating cracks. The formation of cracks in laser cladding coatings is primarily attributed to residual stresses. While existing equipment can measure residual stress, the process is intricate, challenging, and costly. To overcome this limitation, scholars have conducted relevant studies using numerical simulations. Fang et al. [19] reviewed physical models of residual stresses for defects in selective laser melting (SLM) and machined parts, analyzed the advantages and disadvantages of mainstream models, and proposed conceptual methods to enhance residual stress management. Sanaei et al. [20] discussed characterization methods and statistical analysis of coating defects in additive manufacturing (AM), summarizing the effects of process parameters and post-processing on defects. Cheng et al. [21] reviewed the simulation techniques for grain growth mechanism, temperature, and stress distribution in the melt pool directly related to defect formation in the laser metal deposition (LMD) technique. Additionally, the defect suppression methods and the performance improvement methods of filled layers in LMD technology are presented.
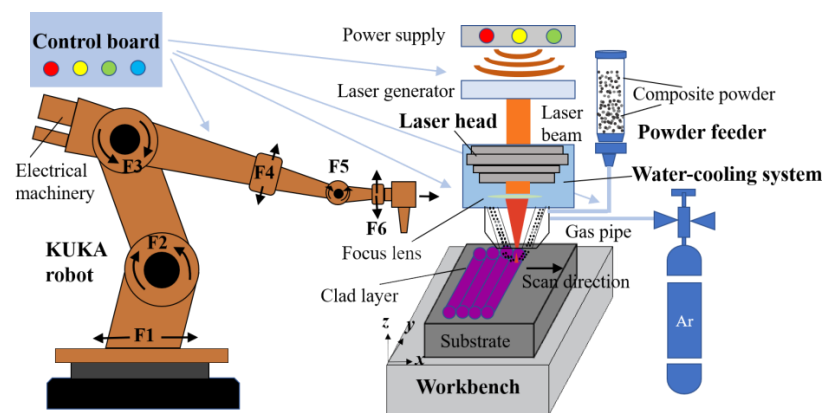
Figure 1. Schematic diagram of the laser cladding system.

In summary, while numerous scholars have provided an overview of crack generation mechanisms and control methods for coatings, there has been limited analysis of the types, formation mechanisms, and control methods of various internal cracks in laser melting coatings. This article comprehensively lists the types of internal cracks in laser cladding coatings from the perspectives of experiments and numerical simulations. The formation mechanisms of coating cracks are elucidated, and a comparative analysis of different control methods for coating cracks is provided. Furthermore, future control methods and new technologies for addressing cracks in laser cladding coatings are discussed, offering valuable insights for crack control and improvement in coating quality in laser cladding processes.

2. Types and Causes of Cracks

2.1. Types of Cracks

Laser-clad coatings exhibit various types of cracks, which can be attributed to the selection of different cladding materials and process parameters. To effectively address the cracking issue in laser-clad coatings, it is crucial to identify the types of coating cracks and understand their causes. To address the issue of the types of cracks in laser-clad coatings, they can be classified as hot and cold cracks according to the time, temperature, and fracture characteristics of the coating cracks, and most of the coating cracks are cold cracks [22].

Hot cracks mainly occur above the solidification temperature line, and their sections have a distinct oxidation color and no metallic luster (Figure 2a). For example, most of the common types of cracks in melt layers, such as austenitic stainless steels, are hot cracks [23]. Hot cracks sprout from hot tearing and are easily influenced by microstructure [24]. Partition of low melting point elements such as Si and C in the molten layer [25,26], inhomogeneous distribution of coarse and brittle phases of compounds and impurities [27], and disordered grain growth are the main factors for the formation of hot cracks [28]. This

is due to the fact that the liquid metal in the melt pool has a very high temperature, so the liquid metal is componentlessly subcooled at the beginning of solidification, and therefore large tensile stresses are formed at the coarse eutectic tissue at low melting points. The tensile stress pulls the solidified tissue partially along the grain boundary, resulting in not enough liquid phase to fill the tissue gap, thus producing cracks. Therefore, thermal-type cracks mostly show cracking characteristics along the grain [29].

Cold cracks mainly occur below the solidification temperature line, and the fractured section of cold cracks appears relatively smooth with a metallic luster (Figure 2b). Cold cracks often involve secondary crack generation, indicating a brittle fracture behavior. For instance, nickel-based alloy powder coatings commonly exhibit cold cracks [30]. Improper selection of melting process parameters and excessive thermal gradients in the melt pool are the main factors contributing to cold crack formation. This is due to the susceptibility of martensitic phase transformation at the solidification temperature line [31], leading to the hardening of the coating. The differences in thermal–physical parameters between the cladding material and the substrate material, coupled with the cooling and solidification process, result in the generation of large residual thermal stresses. When these residual thermal stresses surpass the tensile strength limit of the material, cold cracks occur [31–33]. Consequently, cold cracks typically exhibit crack propagation through the crystal structure [34].
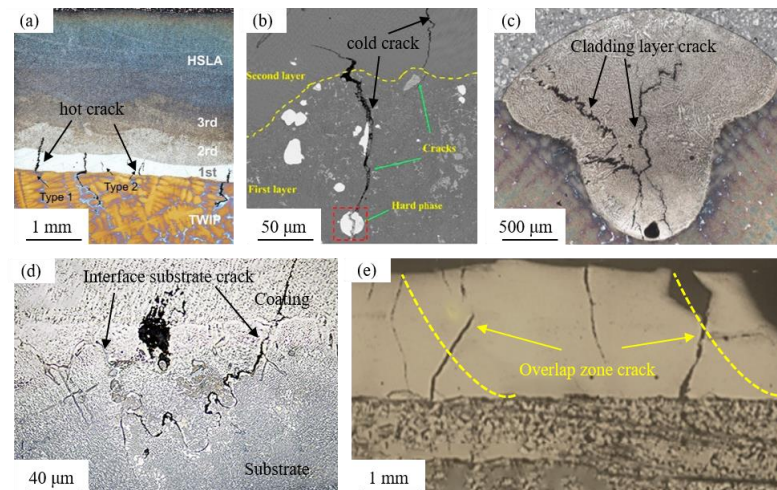
Figure 2. Different types of crack morphology. (**a**) The hot cracks in HSLA powder samples (the laser power is 2900 W and the scan speed is 10 mm/s) [25]; (**b**) the cold cracks in Ni-Cu alloy sample (the laser power is 5000 W and the scan speed is 30 mm/s) [35]; (**c**) cladding layer crack in ZhS32 alloy (the laser power is 600 W and the scan speed is 9 mm/s) [36]; (**d**) interface substrate crack in nickel-based K477A (the laser power is 576 W and the scan speed is 4 mm/s) [37]; (**e**) overlap zone crack in Ni60 (the laser power is 3200 W and the scan speed is 416.7 mm/s) [38].

Depending on their location, coating cracks can be classified as fusion layer cracks, interface substrate cracks, and overlap zone cracks [37–39].

Cladding layer crack is caused by rapid cooling during the solidification process, leading to significant thermal stress. Uneven stress distribution resulting from the uneven mixing of cladding material or the presence of impurities can also contribute to the cracking of the cladding layer (Figure 2c). When cracks form within the clad layer, they often initiate near hard-phase particles and propagate vertically through the coating. In some cases, the cracks even extend into the substrate. When cracks reach the surface, they exhibit a "herringbone" or lattice-like pattern [34,39].

Interface substrate crack primarily arises from the excessive difference in thermal expansion coefficient and Young's modulus between the substrate and the molten cladding layer. This difference creates thermal stresses under large temperature gradients during solidification and cooling. Additionally, the molten metal liquid experiences restraint stress from the substrate during thermal expansion and cooling contraction. As a result of the

combined effects of thermal and restraint stresses, cracking occurs at the interface between the clad layer and the substrate, gradually propagating to the surface of the molten cladding layer (Figure 2d) [37], forming interface substrate cracks.

Overlap zone cracks predominantly occur in the lap zone as a result of an unreasonable selection of the overlap rate. This leads to the accumulation of heat, an increase in temperature gradient, and elevated thermal stress. Consequently, the grain growth time is prolonged, resulting in coarser grains, as well as the formation of pores or impurities. The expansion of these defects eventually leads to the development of lap zone cracks (Figure 2e). Moreover, the low yield strength and tensile rate of the clad material make it more susceptible to cracking and expansion under combined stress. Consequently, overlap zone cracks tend to propagate throughout the entire fusion cladding layer once they form [40,41].

In summary, hot cracks are mainly caused by hot tearing and are significantly influenced by the microstructure of the coating. The presence of coarse brittle phases and impurities in the molten clad layer, along with thermal cycling and stress concentration due to the shaped orientation of grain boundaries, are the key factors contributing to the formation of hot cracks. Cold cracks, on the other hand, are mainly a consequence of improper selection of process parameters and excessive temperature gradients, resulting in brittle fractures due to tensile stresses exceeding the tensile strength of the molten material. Cracks in the cladding layer arise from the uneven distribution of coating tissue and a substantial difference in the thermal expansion coefficient of the cladding layer. Interface substrate cracks primarily occur due to the excessive temperature gradient between the substrate and the clad layer. Overlap zone cracks, finally, are predominantly caused by inappropriate overlap rate selection. These different types of coating cracks can be analyzed based on their causes of formation, with the strain generated during the melting process being greater than the plastic strain of the molten layer itself, serving as the fundamental cause of coating cracks.

2.2. Causes of Cracks

The laser cladding process is very complex, and the coating generates significant stresses during the cladding and cooling process. When the stresses in the coating exceed the yield limit of the coating material, they can lead to cracking of the coating. The formation of cracks in laser-clad coatings can be attributed to the presence of residual stresses, which can be categorized into three primary types: thermal stresses, organizational stresses, and restraint stresses (Figure 3) [42–44].
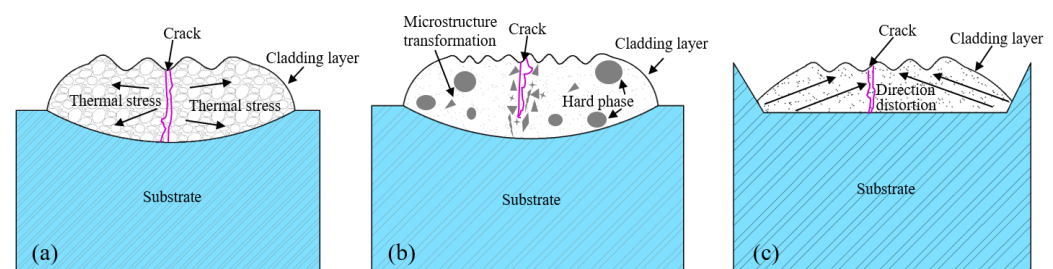
Figure 3. Schematic of principle of three different stress: (**a**) thermal stress; (**b**) organizational stress; and (**c**) restraint stress.

2.2.1. Thermal Stress

The presence of thermal stress in laser-clad coatings can be attributed to the disparate modulus of elasticity and coefficient of thermal expansion between the substrate and the clad material. This results in varying rates of thermal expansion and cooling contraction within the clad layer. When a temperature gradient exists, the clad layer experiences stress, known as thermal stress (Figure 3a) [45]. If the thermal stress surpasses the material's yield limit, it can give rise to cracks in the coating. The calculation of thermal stress involves determining the extent of the stress [45].

$$\sigma_T = \frac{E \times \Delta\alpha \times \Delta T}{1 - \nu} \tag{1}$$

E is the elastic modulus of the cladding material, $\Delta\alpha$ is the difference in thermal expansion coefficient between the cladding layer and substrate material, ΔT is the difference between cladding temperature and room temperature, and v is Poisson's ratio of the cladding layer.

The relationship expressed in Equation (1) reveals that the Poisson's ratio of the molten layer decreases as the thermal expansion coefficient difference between the molten layer and the substrate material increases. Consequently, a larger temperature difference leads to greater thermal stress, making the coating more susceptible to cracking [46]. Because the substrate is difficult to replace in the selection process, and the coefficient of thermal expansion and Young's modulus of the cladding material also differ greatly, the selection of cladding material is particularly important. For instance, when the coating material consists of ceramic particles and the substrate is made of a metal alloy, the distinct thermophysical properties of these materials can cause cracking if the number of ceramic particles added is not carefully chosen. To address this issue, the composition of the cladding layer is commonly adjusted to alleviate the impact of thermal stress [47].

2.2.2. Organizational Stress

During the solidification and crystallization process of the liquid metal within the molten pool, a rearrangement of the physical phase structure takes place, resulting in the generation of internal stress known as organizational stress (Figure 3b) [48]. As thermal cycling progresses, the organizational stress accumulates until it reaches the yield strength of the material. This accumulation of stress can lead to tissue damage, the formation of microscopic defects, and even the development of microcracks, ultimately resulting in brittle fractures. Griffith introduced and refined a model that relates brittle fracture strength to material properties and damage [48], which can be expressed as follows:

$$\sigma_f = \sqrt{\frac{E\left(2\gamma + \gamma_p\right)}{\pi C_z}} \tag{2}$$

E is the modulus of elasticity, γ is the material surface energy, γp is the microcracks or micro defects expanding the plastic work per unit length, C_z is the size of the microcracks and micro defects.

The fracture surface energy γ is about $\frac{aE}{100}$, a is the lattice distance of the crystal; the plastic work γp is 2~3 orders of magnitude larger than γ.

The fracture strength of a material can be estimated by considering the size of the microcrack and the average lattice distance, although the specific value varies depending on the crystallographic system. For instance, in laser-fused coatings containing hard phases such as Cr_7C_3 and $Cr_{23}C_6$, when the size of the microdamage crack within the coating ranges from 3 to 5 µm, the calculated fracture strength (denoted as "σ_f") is approximately 4.4 GPa [49]. When the stress in the coating exceeds this fracture strength, the microcrack extends and develops into macroscopic cracks. Hard phases are generally added to the coating to improve its performance, resulting in poor fluidity of the coating and uneven powder mixing. Therefore, the coating, after melting, is prone to elemental segregation. The presence of elemental segregation contributes to an inhomogeneous phase transition structure, resulting in stress concentration and elevated organizational stresses. Ramakrishnan et al. [50] proposed that Inconel 738 coating cracking occurs due to the micro-segregation of aluminum (Al) and titanium (Ti) elements, as well as the presence of low melting point crack boundaries.

The concept of micro-bias is directly associated with the diffusion coefficient of liquid alloying elements in the melt pool. This diffusion coefficient can be determined using Formula (3) [51].

$$K = A \times e^{\frac{E}{RT}} \tag{3}$$

K is the rate coefficient, E is the activation energy, T is the absolute temperature, A is the frequency factor, and R is the ideal gas law constant.

The relationship expressed in Formula (3) reveals that an increase in the cooling rate leads to a decrease in the diffusion coefficient of elements, resulting in reduced microscopic

segregation and decreased crack sensitivity. To mitigate these effects and minimize organizational stress caused by uneven phase transformation, various approaches can be employed. These include implementing auxiliary fields, refining the size of the hard phase, or selecting appropriate process parameters. These measures help slow down elemental segregation and promote a more uniform phase distribution within the material.

2.2.3. Constraint Stress

During laser cladding, as the molten cladding layer undergoes heating and expansion or cooling and contraction, hindering stress arises from the un-melted portion on the melted part, referred to as restraint stress (Figure 3c) [52]. Two types of restraint stresses can be identified: the first is compressive stress resulting from the thermal expansion of the initially melted material in the melt pool, constrained by the colder surrounding substrate; the second is tensile stress generated as the molten liquid metal is held by other colder parts of the substrate during condensation and cooling shrinkage.

The constraint stress mainly comes from the constraints of the matrix, so the constraint stress at the edge of the cladding layer is relatively small and less prone to cracking. Research indicates that the middle section of the molten cladding layer is particularly susceptible to cracking due to heat accumulation and limited heat dissipation area, thus requiring additional constraints [53]. Appropriate heat treatment techniques can help reduce restraint stress [54]. In addition, the use of low transformation temperature (LTT) alloys can effectively reduce the accumulation of tensile stress. This is because the low transformation temperature alloy can use the expansion of martensite transformation to offset part or all of the heat shrinkage, thereby reducing the residual tensile stress [55]. However, it is important to note that the melting and cooling behavior of the laser cladding pool is highly complex, and residual stresses are challenging to eliminate entirely. The non-uniform distribution of temperature, stress, and flow fields within the melt pool exacerbates residual stresses, especially when there is a significant temperature gradient or a mismatch in the thermal expansion coefficient and elastic modulus between the molten material and the substrate. Consequently, regulating thermal stress, organizational stress, and restraint stress during the laser cladding coating process, minimizing the individual or interactive effects of these stresses, and preventing or eliminating coating cracking remain significant challenges in current research.

3. Crack Control Method

To address the issue of cracking in laser-clad coatings, this paper provides a comprehensive review of several strategies aimed at controlling crack formation. These methods include the preferential selection of clad layer materials [56–58], optimization of coating process parameters [59], implementation of increased heat treatment [46], utilization of auxiliary fields [60,61], and the use of numerical simulations [62]. Furthermore, this review highlights recent advancements and novel approaches in the field, summarizing the progress made in controlling coating cracking in recent years.

3.1. Preferred Cladding Material

3.1.1. Control of Hard-Phase Content in the Cladding Layer

There are many applications of laser cladding, among which the most prominent application is the preparation of surface-strengthening coatings to improve the hardness and wear resistance of parts. It has been demonstrated that the proper addition of hard-phase particles with high melting points, such as WC, TiC, and ZrO_2, can effectively refine the grains of the coating. This refinement reduces organizational stresses caused by elemental segregation and lowers the susceptibility of the coating to cracking [63]. For instance, Zhao et al. [64] observed that Ni-based WC-CeO_2 coatings exhibited smaller secondary dendrite spacing and were free from cracks compared to Ni-based CeO_2 coatings. This improvement can be attributed to the addition of WC hard-phase particles, which increase the number of carbides in the eutectic structure and refines the grains, thereby enhancing the coating's toughness and reducing its crack susceptibility. However, it is

crucial to control the number of hard-phase particles added, as excessive differences in thermal expansion coefficient and elastic modulus between the coating and substrate can lead to coating cracking. Shen et al. [65] investigated the cracking of NiCrSiBC-WC composite coatings with WC mass ratios of 40%, 50%, and 60% on carbon steel substrates (Figure 4a). The study revealed that the composite coatings with 40 wt.% WC exhibited no cracks, while those with 50 and 60 wt.% WC showed cracks, with significant penetration cracks observed in the middle due to the presence of large grains of WC.

Similar observations have been made regarding the effect of hard-phase particle content on the surface quality and structure of coatings. Shen et al. [66] studied the cracking of NiCrSiBC-WC composite coatings and found that coatings with 30–40 wt.% WC exhibited no cracking or fragmentation of WC particles, whereas coatings with 50–60 wt.% WC exhibited significant deterioration and increased cracking. This can be attributed to the fact that the secondary precipitation phases of WC, such as bulk carbides and rod carbides (laminated carbides), have poor wetting properties with nickel and are highly susceptible to stress concentration, leading to cracking [46]. Similarly, Liu et al. [67] investigated the effect of TiC volume fraction on the microstructure and tensile properties of TiC/TA15 titanium-based composite coatings. They discovered that composites with 5 vol.% TiC exhibited improved strength, whereas the tensile properties deteriorated as the TiC volume fraction increased, resulting in coating cracking. Similarly, Ignat et al. [47] found that when the volume fraction of ZrO_2 in the coating exceeded 15%, the surface quality of the coating deteriorated with the appearance of cracks.
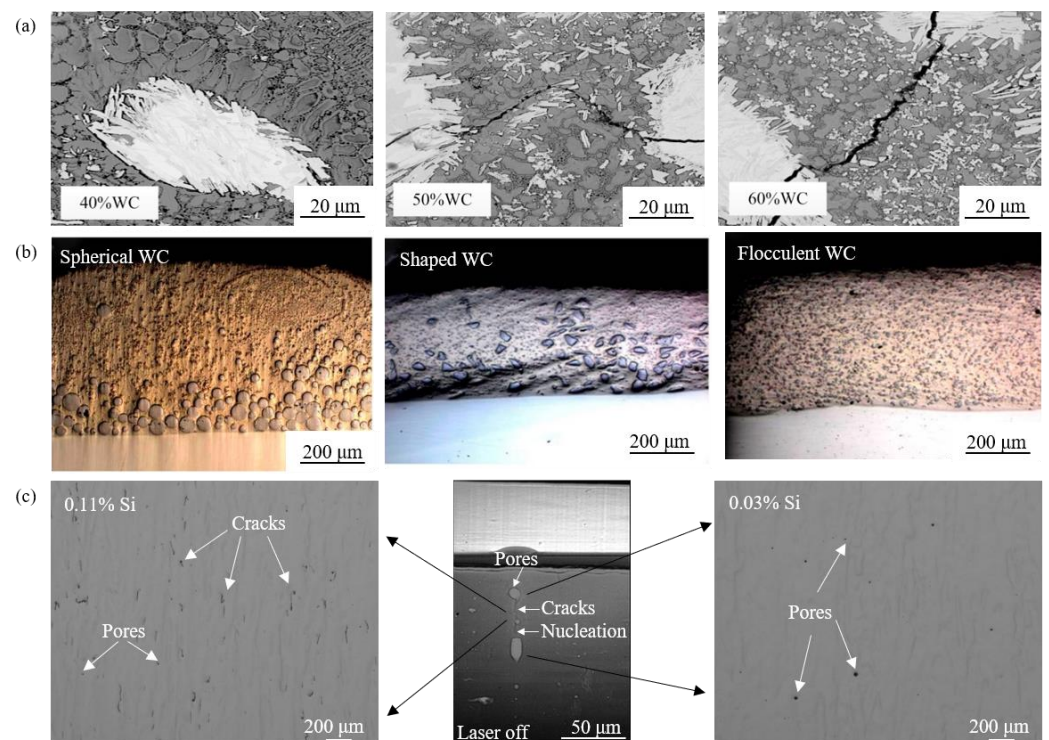
Figure 4. The effect of cladding materials on the microscopic morphology of coatings. (**a**) Micromorphology of NiCrBSi-WC coatings with different WC contents [65]; (**b**) microscopic photos of different types of WC coatings in Ni60-30 wt.% WC composite coatings [68]; and (**c**) microscopic photos of coatings with different silicon contents in IN738LC coatings [69].

In summary, when incorporating ceramic hard-phase particles into the coating, it is important to limit the hard-phase content. The commonly used WC ceramic particle content should be kept below 50 wt.%, and the content of other less dense hard-phase particles should also be controlled. Otherwise, excessive stress may lead to cracking in the coating.

3.1.2. Preferred Hard-Phase Particle Type

Hard-phase particles can be categorized into microns and nanoparticles based on their particle size [70]. They can also be classified as spherical, shaped, or flocculent based on their shape [68]. Furthermore, hard-phase particles can be classified according to their structure as mechanically mixed or encapsulated [71]. The addition of different types of hard-phase particles results in variations in coating properties and the occurrence of coating cracks, and the choice of preferred hard-phase particles can enhance the crack resistance of the coating.

Regarding the impact of hard-phase particle size on coating cracks, researchers have found that larger particles can impede crack expansion. However, when the particle size is excessively large, it can lead to stress concentration and subsequent coating cracking [72]. He et al. [73] investigated the influence of micron and nano-sized TiC particles on the structure and properties of TiC-TiAl composite coatings. They discovered that the coating containing 20 wt.% micron-sized TiC had 14 cracks, while the coating with 10 wt.% nano-sized TiC had only 6 cracks, and the coating with 20 wt.% nano-sized TiC had a mere 3 cracks. Wang et al. [74] observed the elimination of cracks near the substrate interface upon the addition of 1 wt.% nano-sized Al_2O_3 to NiCoCrAlY high-temperature protective coatings. Li et al. [75] further demonstrated that nanoceramic particles not only eliminated coating cracks but also transformed columnar crystals into equiaxed crystals with a more uniform and dense structure.

In terms of the influence of hard-phase particle shape on coating cracking, Zhang et al. [68] investigated the effect of spherical, shaped, and flocculent WC particles (30 wt.%) on Ni60 coatings. They found that spherical WC particles mainly accumulated in the lower-middle part of the coating, while shaped WC particles showed a similar distribution pattern. In contrast, smaller flocculent WC particles were uniformly dispersed throughout the coating (Figure 4b), and coatings prepared with flocculent WC particles exhibited a smaller tendency to crack.

Regarding the impact of hard-phase particle structure on coating cracks, mechanically mixed WC particle coatings in a Ni-based substrate commonly exhibit cracking, whereas coatings prepared with overlapping particles such as WC-Co and WC-Ni demonstrate overall improved performance. Zhang et al. [76] observed that four Ni-Cu/WC-12Co composite coatings with WC-12Co content ranging from 0 to 30 wt.% showed no cracks. Similarly, the WC-Ni coating prepared by Tehrani et al. [77] was not only crack-free but also 1.5 times tougher than the WC-Co thermal spray coating.

In summary, the proper addition of nano-sized hard-phase particles can refine the grain structure of the coating and enhance its toughness. Flocculent hard-phase particles can be evenly distributed within the coating, thereby preventing stress concentration caused by particle aggregation. Encapsulated hard-phase particles possess good mobility and wettability, improving the coating's toughness and playing a stronger role in reinforcement while impeding crack expansion. Therefore, when selecting the type of hard-phase particles, consideration should be given to their particle size, shape, and structure.

3.1.3. Adding Alloying Elements

Studies have demonstrated that the presence of excessive residual stress in the coating can lead to brittle cracking. However, the addition of alloying elements such as Co, Cr, Si, and V_2O_5 to the coating can enhance fracture toughness and reduce its susceptibility to cracking.

In a study conducted by Dai et al. [78] on the effect of Co content on the cracking susceptibility of WC/Fe laser-clad layers, it was observed that the toughness of the coating increased with the addition of Co. When 8 wt.% Co was added, the toughness reached nearly 1100 MPa, which was 1.3 times higher than the coating without Co. Hence, the addition of the Co element effectively mitigates the tendency of the coating to undergo brittle fracture and exhibits favorable toughening and plasticizing effects. Qi et al. [79] investigated the mechanism behind the improvement in coating cracking through the addition of the Cr element. They found that the presence of Cr gradually refined the coating grains (Figure 4d). Moreover, the addition of the Cr element positively influenced the reduction in the elastic modulus of the clad layer, thereby enhancing the coating's toughness and alleviating thermal stress and solidification shrinkage in the clad layer,

ultimately reducing the susceptibility to coating cracking. Sun et al. [69] observed a crack density of 0.85 mm/mm for an IN738LC high-temperature alloy coating with a 0.11 wt.% Si content, whereas the sample with 0.03 wt.% Si content exhibited minimal cracking and only a few pores (Figure 4c), consistent with the findings of Cloots et al. [24]. Wang et al. [23] noted that high volume fraction and uneven distribution of hard phases such as chromium boride and carbide in NiCrBSiC coatings resulted in thermal stress concentration. However, the addition of V_2O_5 led to grain refinement, improved coating toughness, reduced crack sensitivity, and the elimination of cracking when added at 5 wt.%.

In summary, the addition of alloying elements aims to enhance the toughness of the coating, increase its yield limit, and transition it from a brittle to more ductile behavior. Furthermore, it promotes grain refinement and uniform distribution within the coating to avoid stress concentration, thereby reducing the coating's susceptibility to cracking.

3.1.4. Addition of Rare Earth Oxides

Studies have revealed that the incorporation of rare earth elements, such as La, Ce, and Y, which exhibit surface active properties, can effectively reduce the surface tension of molten metal during coating formation. This reduction in surface tension improves the mobility of the melt pool, consequently minimizing defects such as porosity and cracks in the coating [16]. For instance, Sun et al. [80] synthesized (Ti, Nb) C/Ni coatings through in situ synthesis and investigated the impact of CeO_2 additions ranging from 0 % to 9 wt.% on the coatings' microstructure and defect formation. It was observed that coatings without CeO_2 or with excessive CeO_2 additions displayed more pores and cracks, whereas the addition of 5 wt.% CeO_2 significantly improved the microstructure.

Moreover, rare earth elements undergo chemical reactions with impurity elements (e.g., S, O, Si, and N) upon thermal decomposition, leading to the formation of stable high melting point compounds that serve as crystalline nuclei. This process increases the number of nucleation sites, resulting in a greater number of grains and a refined coating structure. Consequently, the toughness of the coating is enhanced, and defects within the coating are reduced [81]. Table 1 presents the impact of different rare earth oxides on the improvement in coating cracks.

Table 1. Improvement effect of different types of rare earth oxides on coating cracks.

Coating/Substrate	Rare Earth Oxide wt.%	Improvement Effect
Fe-based/5CrNiMo [82]	1%/2%/3% Y_2O_3	A 2% Y_2O_3 coating was added without cracks or pores
TiB-TiC/Ti6Al4V [83]	2% Y_2O_3	The average fracture toughness was increased from 8.32 MPa $m^{1/2}$ to 17.36 MPa $m^{1/2}$, and the cracking resistance was improved
Ni-based/45 steel [84]	0.1%–1% La_2O_3	The addition amount was 0.6%; the coating had no cracks, and the microstructure was refined
Ni-60%WC/ASTM A36 [85]	0.5%–2% La_2O_3	A 1% La_2O_3 was added; the coating was tight and defect free When the addition amount was greater than 1.5%, the oxygen content increased, and defects increased
Ti/Ti6Al4V [86]	1% CeO_2 and 1% Y_2O_3	Refined the coating structure and ensured that the coating had no defects
CrTi4-TiCx/Ti6Al4V [87]	1%–4% CeO_2	The addition amount is 2%; the coating has no cracks
Ni60A/TC4 [88]	1%–4% CeO_2	The fluidity of the molten pool improved, and the addition amount is 3%; there are no obvious cracks in the coating
Ni60/6063Al [89]	5% Y_2O_3, CeO_2, and La_2O_3	Dense organization, refined grain size, without obvious cracks and pores

In summary, the selection and quantity of rare earth oxides added vary depending on the specific molten coating material, typically within a controlled range of 5 wt.%. Notably,

when the addition of rare earth oxides falls between 0.5 and 2 wt.%, the resulting coating exhibits a dense structure with small grains and minimal observable defects. Excessive addition of rare earth oxides leads to increased oxygen content within the coating and the introduction of impurities at grain boundaries, thereby exacerbating defect formation. Hence, strict control over the addition of rare earth oxides is crucial.

3.1.5. Adding a Transition Layer

Transition layers in laser cladding coatings can be classified into two categories. The first category is the buffer layer, which possesses thermophysical properties like the substrate. This buffer layer acts as an intermediary between the cladding layer and the substrate, reducing the residual stress in the coating and minimizing the dilution effect caused by the substrate [90]. The second category is step coating. In cases where the melt layer contains a high concentration of hard-phase particles, a layer-by-layer incremental approach can be employed to incorporate the hard-phase particles and alleviate the residual stresses between different layers of the coating [91,92].

In studies focusing on buffer layers for stress reduction in coatings, Cao et al. [93] successfully prepared Cr_3C_2-reinforced Ni60A-Ag self-lubricating composite coatings on a copper alloy substrate using a NiCr buffer layer. This approach effectively addressed issues related to segregation and cracks caused by coarse Cr_7C_3 columnar grains in single-layer composite coatings. Similarly, through pre-coating a CoCrFeMnNi melt layer on the substrate, Zhang et al. [94] achieved the successful formation of a 5–20 wt.% TiC composite-reinforced coating, which reduced stress concentration and enhanced the coating's resistance to cracking. Thawari et al. [95] utilized an Inconel 625 buffer layer to deposit a wear-resistant Stellite 6 coating on an SS316 substrate, resulting in a coating with reduced defects such as porosity and cracks. The buffer layer prevented direct contact between Stellite 6 and the substrate, thereby minimizing the temperature gradient (G) and slowing down heat loss in the molten layer.

Regarding the reduction in stress in step fusion coatings, Paul et al. [71] employed a pulsed Nd: YAG laser to deposit multilayer heavy gradient fusion layers on a mild steel substrate. This approach effectively addressed issues such as cracks, porosity, poor bonding, and partial melting of WC particles in the Co substrate. Wang et al. [96] utilized a gradient combination design in the preparation of WC-enhanced nickel-based gradient composite coatings, significantly reducing the susceptibility to cracking in coatings with a high concentration of hard-phase particles. Similarly, Li et al. [97] successfully prepared crack-free 50 wt.% TiC-Ti6Al4V composite gradient coatings using a similar approach.

In summary, the buffer layer serves as a buffer to mitigate cracking issues in composite coatings with a low concentration of hard-phase particles. On the other hand, step coatings are employed to address cracking problems in composite coatings with a high concentration of hard-phase particles. For instance, when the ceramic addition exceeds 50 wt.%, a multi-layer step fusion coating should be selected to alleviate stress between the coatings and reduce the susceptibility to cracking.

3.2. Optimization of Cladding Process Parameters

3.2.1. Main Process Parameters

The primary process parameters of laser cladding encompass laser power (*P*), scanning path, scanning speed (*V*), powder feed (F), powder thickness (H), spot diameter (*D*), overlap rate (O), and more. Among these parameters, laser power, scanning speed, and spot diameter are interconnected and have a comparable impact on the cracking behavior of the coating. To explore the relationship between laser power (*P*), scanning speed (*V*), spot diameter (*D*), and the coating's cracking behavior, the concept of laser energy density *E* was introduced [98]:

$$E = \frac{P}{DV} \tag{4}$$

From Formula (4), it can be seen that E is positively correlated with P and E is negatively correlated with D and V. The process parameters of common cladding material systems and their effects on the cracking behavior are shown in Table 2.

Table 2. Relationship between process parameters and crack behavior.

Coating/Substrate	Process Parameters	Influence Law
Ni60/40Cr [99]	P: 1000–1800 W, V: 20–25 mm/s, F: 80 r/min, D: 4 mm, O: 50%, and defocus: 0–4 mm	P: 1000–1800 W, the crack rate decreased from 0.2 to 0.11 N/mm. Defocus: 0–4 mm, the crack rate increased from 0.1 to 0.23 N/mm.
FeCoCrNi/ TC4 [63]	P: 800–1050 W, V:8–12 mm/s, H: 0.5–1 mm, and D: 2 mm	When the heat input and H increased, the cracking first decreased and then increased. When H was 0.75 mm, the crack rate was the lowest. The influence of P and V on crack rate was much greater than that of H.
TiC/mild Steel [100]	P: 1000–2800 W, V: 4 mm, and D: 0.5 mm	Under four laser powers, the coating had no cracks or pores, the heat input was large enough, and the coating had no cracks.
WC-Co/ Cr-Mo-V [101]	P: 600–1000 W, F: 4–30 g/min, D: 2 mm, and nitrogen and argon gas protection atmosphere	When F was higher than 5 g/min, the coating was discontinuous and had defects; under nitrogen protection, all samples had cracks and pores; and under argon protection, all samples had no cracks.
7055AA/ 2024AA [102]	P: 1200–2000 W, V: 10–30 mm/s, D: 2 mm, linear pattern, and two types of arc pattern cladding	The larger P was, the smaller V was, and the greater residual compressive stress was; the residual stress in linear mode was minimized, and the optimal solution was obtained when the cladding angle was 0°.
StelliteX-40/ GH4133 [103]	P: 1000–3000 W, V: 5–8 mm/s, H: 0.6–1.2 mm, 750 °C, and 16 h annealing treatment	P: 1000 W, the coating was not fused; P: 3000 W, reheat cracks appeared; H > 1.1 mm, the coating was not melted; and after treatment, only 3000 W coating had intergranular reheat cracks.
Inconel 690/ Inconel600 [104]	P: 2000–3000 W, V: 12–16 mm/s, D: 5 mm, and 25–300 °C preheating	P was too small, or F was too large, leading to poor coating quality; increasing P, decreasing F, and preheating could reduce defects.
Ni60/45 Steel [105]	P: 1600 W, V: 5–11 mm/s, F: 15–21 g/min, O: 45–60%, and defocus: 16 mm	When F increased, the crack rate increased; when overlap rate increased, the crack rate increased; the larger the V, the greater the crack rate.

Here are the revised and retouched paragraphs regarding the recommendations for improving coating cracks:

(1) Increase the laser power appropriately, and reduce the spot diameter and scanning speed. When the laser energy density (E) is low, the molten coating powder may not melt sufficiently, leading to an increased rate of coating cracking. Increasing the laser energy density (E) ensures sufficient melting of the metal in the molten pool, reducing the susceptibility of the coating to cracking [106,107];

(2) Adjust the thickness of powder laying and the amount of powder feeding appropriately. Increasing the thickness of powder laying and the amount of powder feeding results in a larger amount of metal being melted. If the laser energy is insufficient to melt all the powder, it can lead to impurities, pores, coarse coating structure, and, ultimately, cracks. However, reducing the amount of powder feeding or powder thickness too much may result in overburning, thermal deformation of the substrate, and reduced coating quality [105];

(3) Set the overlap rate reasonably. Excessive overlap can cause heat buildup, leading to increased thermal stress and higher susceptibility of the coating to cracking. Conversely, a very low overoverlap rate can result in a discontinuous coating surface and the formation of defects. To ensure high-quality coating formation, the overoverlap rate is generally chosen to be within the range of 30% to 60% [108].

Additionally, the scanning path employed can also impact coating stresses, consequently affecting the propensity for coating cracking. Saboori et al. [109] analyzed the effect of four main scanning strategies (raster, bi-directional, offset, and fractal) on the residual stresses in the final coating. They observed different residual stresses in coatings produced with different scanning paths. For instance, the use of the offset-out scanning strategy reduced the coating residual stresses to one-third of those produced by the bi-directional scanning strategy [110].

3.2.2. Other Process Parameters

In addition to the primary process parameters such as laser power, scanning speed, and powder feed, other factors such as laser parameters (pulse frequency and pulse width)

and the external environment (protective atmosphere and incidence angle) can also impact the occurrence of coating cracks.

Decreasing the pulse frequency and increasing the pulse width have been found to reduce coating crack defects. Javid et al. [111] observed a decrease in the number of coating cracks as the pulse width increased. This is attributed to the fact that a wider pulse width results in a lower cooling rate, increased dilution rate, decreased residual stresses, enhanced coating toughness, and reduced susceptibility to cracking. Ali Khorram et al. [112] investigated the influence of parameters such as pulse width and laser frequency on the occurrence of solidification cracking in coatings. They discovered that high dilution rates and coating thickness cause the formation of longer solidification cracks, while crack-free coatings can be achieved at lower dilution rates (28%). Furthermore, utilizing a lower laser frequency can lower the dilution rate, enabling the preparation of crack-free coatings [29].

Although most studies have focused on laser melting coatings on flat surfaces, the investigation of melting conditions on tilted substrates is still in the exploratory stage. Bowen Shi et al. [113] examined the effect of substrate tilt angle on the cracking behavior of high-hardness Ni60A coatings and observed that the cracking rate increased 3.5 times for up-lap coatings and 4 times for down-lap coatings as the tilt angle increased from 0° to 60°. The cracking mode observed was a quasi-dissociative fracture. Therefore, choosing an upward lap configuration can minimize the shielding and reflection of the laser by the molten coating, leading to increased laser utilization, enhanced melt pool mobility, and reduced coating cracking. Additionally, Yamaguchi et al. [114] discovered that reducing the oxygen concentration can effectively prevent defects such as porosity and decarburization resulting from the carbon–oxygen reaction in the coating. Therefore, using an inert gas such as argon as a protective gas can help reduce coating defects such as porosity and cracks.

3.3. Increasing Heat Treatment

Residual stresses in coatings can be mitigated by employing suitable heat treatment techniques during the laser fusion coating process. Commonly used heat treatments include the preheating pretreatment, slow cooling post-treatment, and laser remelting.

Preheating the substrate can reduce the temperature gradient between the coating and the substrate, thereby lowering thermal stress and decreasing the susceptibility of the coating to cracking (Figure 5a). However, excessive preheating can lead to increased crack length, necessitating careful control of the preheating temperature [29]. Ding et al. [115] conducted experiments using different preheating temperatures on Q460E substrates with 12CrNi2 coatings and developed a finite element residual stress analysis model. Their findings demonstrated that preheating effectively reduces residual stresses in the coatings. Bidron et al. [116] conducted repair studies on CM-247LC high-temperature alloy and determined that using low energy input and an induction preheating temperature close to 1100 °C was highly effective in preventing specimen cracking. Moreover, to address various concerns, Zhou et al. [117] proposed the laser induction hybrid rapid cladding (LIHRC) technique, which solved the problem of substrate damage caused by preheating. This technique not only improved cladding efficiency but also resulted in crack-free composite coatings.

Slow cooling post-treatment mainly involves adjusting the microstructure of the coating and slowly releasing residual stress in the coating (Figure 5b). Li et al. [118] found that the fracture toughness of coatings increased from 2.77 to 3.80 MPa·m$^{1/2}$ at 1 and 2 h of post-treatment with heat retention, thereby reducing the susceptibility to cracking. In another study, Chen et al. [119] investigated the effect of post-melt stress relief treatment on residual stresses in laser melting of AISI P20 tool steel on pre-hardened deformed P20 substrates. They observed that slow cooling post-treatment altered the volume fraction of residual austenite in the coating and significantly reduced residual stresses, consequently reducing the coating's susceptibility to cracking. These findings align with the results reported by Chen et al. [120] and Telasang et al. [121]. Dai et al. [78] found that slow cooling

post-treatment was not as effective as substrate pre-treatment in eliminating cracks, as some cracks had already formed during the cooling process and could not be eliminated.
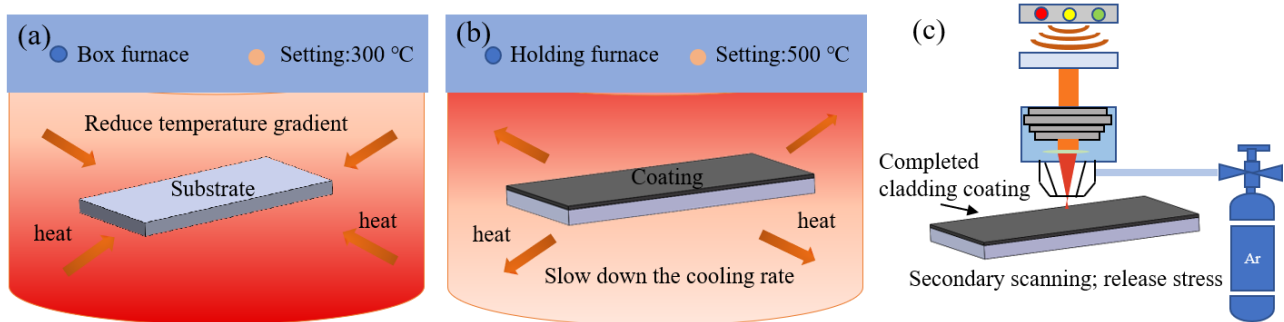
Figure 5. Heat treatments: (**a**) preheating treatment; (**b**) slow cooling post-treatment; (**c**) laser remelting.

Laser remelting is a secondary scanning of the laser cladding coating, which forms a molten pool on the surface of the coating again, thereby releasing coating stress (Figure 5c). Wang et al. [122] prepared iron-based amorphous coatings on H13 steel and observed a significant reduction in coating cracks after laser remelting. Similarly, Lu et al. [123] prepared $Fe_{37.5}Cr_{27.5}C_{12}B_{13}Mo_{10}$ amorphous coatings and found that directly fused coatings exhibited significant cracks, whereas the coatings showed minimal cracks after laser remelting.

In summary, pretreatment is the most effective method for inhibiting coating cracking as it directly reduces thermal stresses. Slow cooling post-treatment functions as a thermal insulation and gradual cooling process to release residual stresses over time. Laser remelting creates a new melt pool on the substrate surface, filling some existing cracks and releasing residual stresses from previous scans. Among the three mentioned techniques, the preheating pretreatment is the most effective in preventing coating cracking. This is because the preheating pretreatment directly reduces thermal stresses. In contrast, post-treatment cannot eliminate existing cracks, and laser remelting may introduce new residual stresses.

3.4. Application of Auxiliary Field

Coating materials and laser coating process parameters have limited direct influence on changes occurring in the melt pool. They can only be adjusted based on process requirements. However, off-field auxiliary technologies have emerged as a popular research topic in recent years to address the cracking problem in laser-clad coatings. These technologies directly impact the energy and mass transfer of the melt pool without physically contacting the coating. They improve the uniformity of the coating structure, reduce elemental segregation, and prevent local stress concentration, thereby slowing down or eliminating defects such as cracks and holes in the coating [85,124–126]. Some commonly studied auxiliary fields include friction stirring, electromagnetic fields, mechanical vibration, and compound fields (Table 3).

Table 3. Effect and mechanism of different auxiliary fields on coating cracks.

Auxiliary Field	Coating/Substrate	Effect	Function Mechanism
Magnetic Field [127]	Co-based/42CrMo	The cracks and pores are reduced; the magnetic field intensity is 20 mT, the magnetostrictive effect is maximum	Magnetostrictive effect can effectively reduce the coefficient of thermal expansion and elastic modulus of cladding layer, and reduce element segregation
Ultrasonic Vibrations [128]	316L/ASTM 1045	Refine the microstructure of the cladding layer, effectively reducing micro defects such as pores and cracks	Vibration causes tissue fragmentation and secondary dendrite fracture, and changes the orientation of the crystal from (220) to (111), resulting in a dense structure

Table 3. *Cont.*

Auxiliary Field	Coating/Substrate	Effect	Function Mechanism
Friction Stir [125]	Ni-Cr-Fe/45 steel	Refines grain size, obtains nanostructured coatings, and eliminates coating cracks	Rapid stirring increases friction heat and strain rate, which is beneficial for toughening and plasticizing
Electromagnetic Field [129]	Ni60/pure iron	The toughness of the coating is improved, and the number of cracks is reduced	Electromagnetic stirring causes Cr_7C_3 to fracture into an independent rod-shaped structure, improving the nucleation rate
Ultrasonic–Electromagnetic Field [130]	NiCrBSi/42CrMo	Refines organization, reduces element segregation, and significantly reduces coating defects	Ultrasonic flow and electromagnetic force stirring cause the dendrites in the cladding layer to be shattered

The electromagnetic field, for instance, can alter the trajectory of charged particles within the melt pool. By using an alternating electromagnetic field, the melt pool can be agitated, and the grains can be crushed. Studies have demonstrated that the magnetic field refines the microstructure of the coating, and magnetostriction significantly reduces the coating's elastic modulus and enhances its elastic recovery. This improvement in crack resistance was observed by Wang et al. [131], who utilized a steady-state magnetic field to assist in melting a nickel-based alloy coating on a pure iron substrate. Without the auxiliary field, five cracks were found on the coating's surface, but as the magnetic induction intensity increased, the number of cracks gradually decreased. When the magnetic induction intensity reached 0.2 T, only two cracks remained.

Ultrasonic vibration-assisted techniques employ ultrasonic cavitation and acoustic flow reinforcement to generate high-frequency and low-amplitude vibrations. These vibrations agitate the melt pool, ensuring a more uniform distribution of elements and stress fields. Zhang et al. [132] prepared a ceramic particle-reinforced iron-based composite coating using ultrasonic vibration assistance and found that the acoustic flow caused by ultrasonic vibration accelerated the melt pool flow, improved heat and mass transfer, and facilitated the formation of nucleation points for ceramic particles. As ultrasonic power increased, the ceramic particles in the coating became finer and more uniform. However, further increasing the ultrasonic power resulted in the agglomeration of fine ceramic particles, increasing the brittleness of the coating and leading to cracking.

Friction stirring involves the application of frictional heat and the coupling effect of plastic deformation on the molten pool, leading to grain refinement and uniform distribution of carbides within the coating. This process enhances the toughness of the coating. Niu et al. [133] employed friction-stirring thermal coupling to eliminate cracks on the top surface of a Ni-16Cr-8Fe alloy coating. They successfully transformed reticulated carbides into nanoparticles dispersed throughout the substrate austenite, thereby improving grain toughness and refinement. Alibadi et al. [134] discovered that the friction stirring-assisted technique outperformed the furnace remelting technique. It not only eliminated defects such as cracks and porosity in the coating but also significantly increased the hardness and wear resistance of the coating.

When it comes to coatings with low ceramic content, a single auxiliary field exhibits a good crack suppression effect. However, for reinforced coatings with high ceramic content, the crack improvement effect is limited. Consequently, researchers have explored composite fields to address this issue. Zhang et al. [135] introduced the ultrasonic–electromagnetic mixed field (UEM) into laser melting (LC) to prepare Inconel 718 + 60 wt.% WC metal substrate composite (MMC) coatings on Inconel 718 substrates. Coatings without assistance exhibited longitudinal and transverse cracks. However, the presence of a single ultrasonic field caused cavitation and a nonlinear effect of acoustic flow, resulting in a more uniform temperature distribution in the melt pool and a reduced temperature gradient. The single UEM field generated two types of Lorentz force in the melt pool, enhancing Marangoni

convection and reducing the temperature gradient, leading to a uniform temperature distribution. The combined effect of acoustic and Lorentz forces assisted by mixed UEM fields reduced the drag force of WC in the melt pool [130,136]. Consequently, a larger stirring effect occurred in the melt pool, significantly reducing temperature inhomogeneity and completely suppressing cracks.

In summary, magnetic field assistance exploits magnetostrictive effects, ultrasonic vibration fields utilize acoustic flow reinforcement, electromagnetic fields employ Lorentzian magnetism for stirring, and friction stirring often involves thermal coupling. While a single auxiliary field can eliminate defects such as cracks and holes in general ceramic composite coatings, a composite field is more effective for reinforced coatings with high ceramic content. Both single-assisted and composite fields primarily aim to stir the melt pool, achieving homogeneous tissue and refined grains. As a result, the toughness of the coating improves, thereby reducing its susceptibility to cracks. Off-site auxiliary technology is of great significance for improving the uniformity of microstructure in coatings, refining grain size, reducing residual stress in coatings, and suppressing coating cracks and pore defects in the future.

3.5. Numerical Analysis

Real-time monitoring of the intricate melting, cooling, and solidification processes within the melt pool during laser cladding coating is challenging through experimental means. However, numerical simulation offers a viable solution by simulating the coupled behavior of temperature, stress, and flow fields. This simulation provides valuable insights for optimizing laser cladding process parameters and predicting the expansion of cracks. By employing numerical simulations, researchers gain a comprehensive understanding of the complex phenomena occurring within the melt pool, enabling them to refine and improve the laser cladding process. Additionally, these simulations aid in predicting and mitigating crack formation and expansion, leading to more reliable and efficient coating outcomes.

3.5.1. Melt Pool and Physical Field Model

Regarding the melt pool model, Kumar et al. [137] developed a three-dimensional Marangoni–Rayleigh–Benard convection model to investigate the impact of process parameters, such as power and velocity, on various aspects of the melt pool. Their study examined the geometry of the melt pool, dilution level, melt pool temperature, and the microstructure formation and scale along the solidification trajectory. The results revealed that enhanced uniformity in melt pool flow reduced porosity, contributing to improved outcomes. Similarly, Chew et al. [138] employed a three-dimensional finite element model to simulate the residual stresses induced by laser coating AISI 4340 powders on a similar substrate material. They also proposed a laser power decay model for the laser–powder interaction zone during coaxial powder feeding. Furthermore, researchers such as Aucott et al. [139], using high-energy synchrotron micrographs, observed the formation and flow state of the melt pool during laser cladding, investigating the temperature-dependent alloy surface tension coefficient to optimize the laser additive manufacturing process.

In terms of the physical field model, Yao et al. [140] confirmed the significant advantages of multi-dimensional high-frequency vibration in laser cladding and provided a basis for revealing the potential mechanism of multi-dimensional vibration on rapid melting and solidification. Figure 6a,b in their work displayed the temperature field and flow field of 2D vibration at 0.45 s. Tian et al. [141] employed the stress-induced solid phase transformation (SSPT) technique to mitigate residual stresses in coatings. They developed a three-dimensional thermodynamic finite element model to analyze stress-induced solid phase transformation and found that SSPT significantly reduced residual stresses in both the transverse and longitudinal directions (Figure 6c). By inducing the transformation of austenite to martensite through melting, the residual stresses were released, resulting in low-stress coatings. This approach offered a novel strategy for crack elimination. In another study, Li et al. [142] established a multi-field coupled three-dimensional numerical model

of IN625 powder laser disc-clad ductile iron. Their comprehensive model revealed the transient evolution of temperature, flow, morphology, and stress fields within the clad layer.
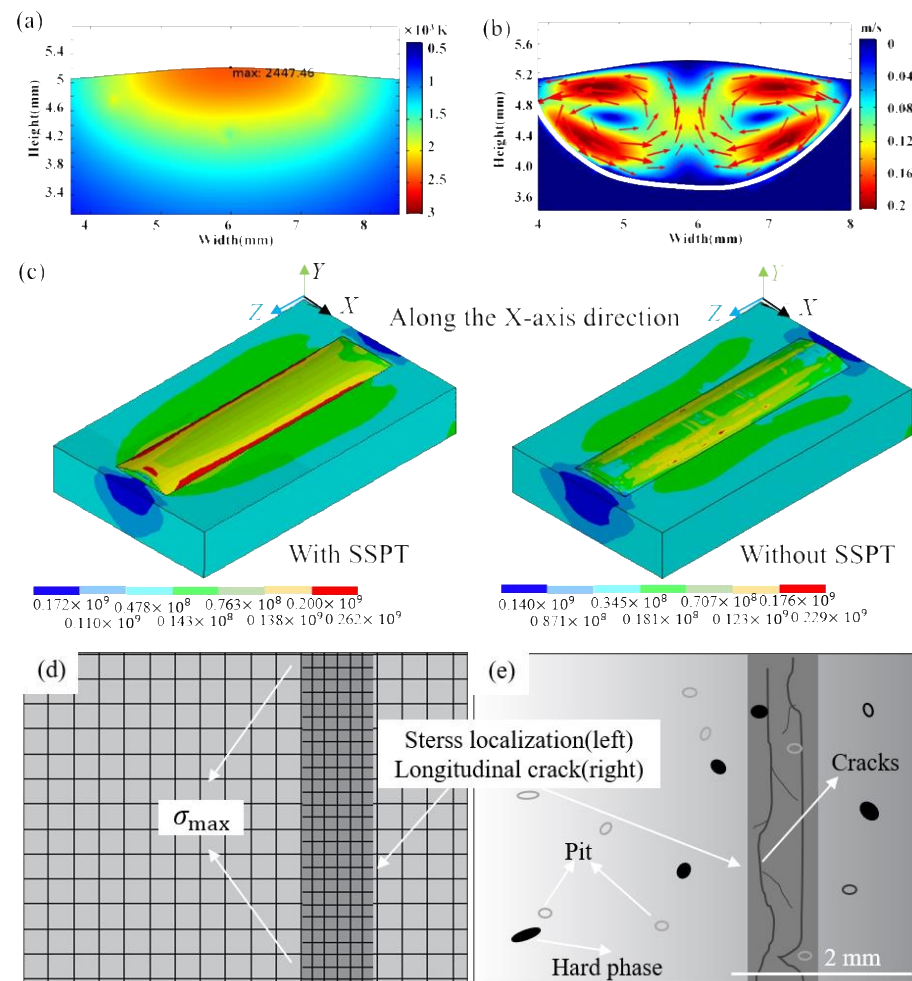
Figure 6. Physical field model and crack prediction. (**a–c**): physical field model (**a**) temperature field with 2D vibration; (**b**) flow field with 2D vibration [140]; (**c**) stress field [141]; and (**d,e**): crack prediction. (**d**) Single channel stress distribution; (**e**) actual distribution of coating cracks.

3.5.2. Process Parameters and Crack Prediction Model

When it comes to simulating laser cladding process parameters, Qiao et al. [143] found through numerical simulation that as the overlap rate increases, the heat accumulation and corresponding maximum residual stress tend to be located at the center of the melted coating, at which point the coating has high crack sensitivity. Yu et al. [105] developed a neural network prediction model that correlated the overoverlap rate, powder feed, scanning speed, and coating crack density. They determined that the sensitivity of coating cracks followed the following order: overoverlap rate > powder feed > scanning speed. Song et al. [102] introduced a dual ellipsoidal heat source-based and sequential-coupled thermal force analysis (SCTMA) method to analyze the distribution of temperature and residual stress fields under different laser power, scanning speed, and laser melting parameters. Their findings indicated that the specimens exhibited minimal residual stresses and the best crack resistance when the laser power was set at 1400 W and the scanning speed was 10 mm/s. The simulated laser melting process parameters can provide the theoretical optimal parameters, save the experimental time for optimizing the process parameters, and facilitate the subsequent theoretical support for the crack prediction model. Regarding the prediction of coating cracks, Li et al. [144] found by ANSYS finite element simulation that a high stress concentration was generated between the coating and the

substrate, which increased the susceptibility to crack formation, and the distribution of transverse residual stress test was basically consistent with the actual crack orientation. Krzyzanowski et al. [145] conducted numerical simulations to analyze the transient fields of thermal and strain–stress during the melting process. The predicted results demonstrated that the equivalent stress in the marked region on the top surface of the single-pass melting layer exceeded the tensile strength limit of the melted material, resulting in the generation of cracks in that region. This observation aligned with the location of longitudinal cracks observed experimentally (Figure 6d,e). Li et al. [146] proposed a method for identifying the state of the cladding layer and detecting cracks during laser cladding. By monitoring the acoustic emission signal during the laser melting process, the presence of cracks in the coating can be determined, along with identifying their location. Cracked clad layers exhibit high-amplitude and high-energy impact signals, whereas the acoustic emission signal collected from uncracked clad layers is more moderate. The crack prediction model is mainly used to obtain the location of cracks by simulating the stress magnitude and distribution, and to identify the cracks in the coating by detecting the acoustic signal when cracks are generated to determine whether cracks exist in the coating.

In summary, numerous numerical simulations of the laser cladding process have been witnessed in recent years. Scholars have analyzed the flow of the melt pool, as well as the temperature, stress, and flow fields during cladding, while investigating the behavior of cracking under different process parameters. Additionally, the proposed prediction models for coating cracks have facilitated the detection and identification of cracks in laser melting coatings, presenting a significant advancement in crack exploration within laser melting coatings.

3.6. Other Methods

To address the issue of cracks in laser cladding coatings, researchers have proposed innovative methods that go beyond numerical simulations and optimization processes. These approaches mainly involve the development of the exploration of novel preparation processes and new structural materials.

In terms of novel preparation processes, Cen et al. [147] proposed a method for suppressing solidification cracks in Al-Cu-Mg alloy during laser melting using high-frequency beam oscillation (Figure 7a). This method effectively reduced solidification cracks, induced a columnar to equiaxed crystal transformation, and minimized coating cracks without requiring additional auxiliary measures. Yang et al. [148] investigated the forming properties and solidification behavior of a high-reflectivity CuCrZr alloy coating on an AlSi7Mg substrate under infrared (IR), blue, and hybrid lasers. Materials with high crack sensitivity exhibited severe cracking and spheroidization tendencies when melted with IR and blue lasers, respectively. However, the use of a hybrid laser source (960 W blue laser + low-power IR laser of 100 and 200 W) successfully produced crack-free coatings (Figure 7b). Zhang et al. [149] implemented a superposition method where two uniform rectangular spots with different sizes and energy densities were used, resulting in the formation of convex spots (Figure 7c). The thermal-force coupling analysis of the McrAlY coating melted with uniform rectangular and convex beam spot processes demonstrated that the convex spot provided preheating and slow cooling effects, reduced the temperature gradient between the substrate and the melted layer, decreased residual stress, and effectively mitigated cracking tendencies in the melted layer.

In terms of novel structural materials, Feng et al. [150] successfully prepared a crack-free Fe-C-B-W-Cr-Nb-V-Si-Mn coating with an ultrafine eutectic structure consisting of shaped nanostructured dendrites. This coating exhibits the high toughness characteristic of nanomaterials without agglomeration. The small microstructure length of the eutectic structure matches the critical crack size, enabling the possibility of crack deflection at the phase boundary. Another study by Wang et al. [151] involved the preparation of a core–shell-structured composite powder consisting of 420 stainless steel powder and nano WC-Co particles using high-energy ball milling. The composite powder exhibited

excellent sphericity and fluidity, making it highly suitable for laser cladding (Figure 6e). Consequently, the application of this core–shell composite powder resulted in the formation of dense coatings with uniform hardness distribution and no cracks.
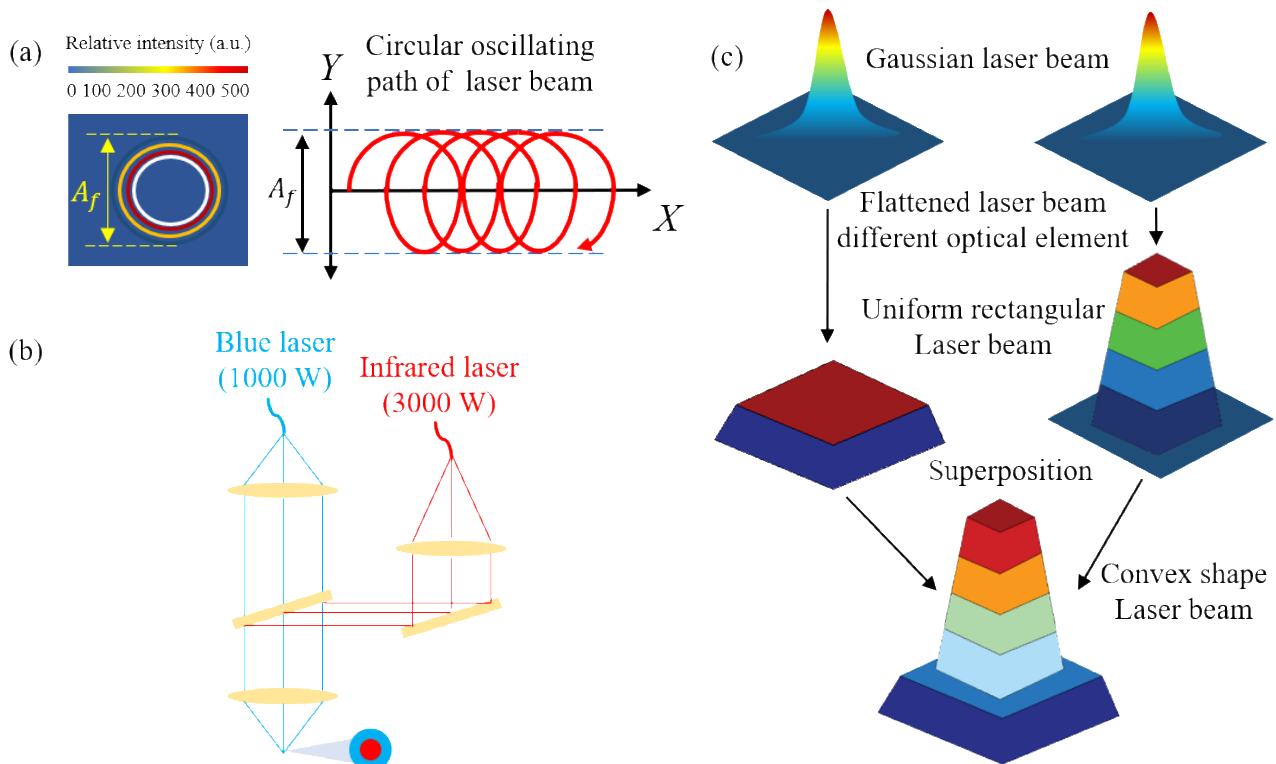
Figure 7. New preparation processes. (**a**) Energy distribution of the circular oscillating laser beam; (**b**) the laser power combination mode; and (**c**) schematic diagram of convex light spots formed by overlapping rectangular light spots.

In summary, researchers have made significant advancements by exploring innovative preparation processes and new structural materials to control cracks in laser cladding coatings. These approaches offer promising strategies for achieving crack-free coatings with improved properties.

3.7. Cracks Control Methods Comparison and Evaluation

In view of the problem that the variety of coating crack control methods is complicated and the practicality is difficult to evaluate, this paper adds a comparative analysis of various control methods, evaluating and analyzing them in terms of control effects, economic benefits, applicability, and other aspects. Table 4 summarizes the practical effects, advantages, and disadvantages of six crack control methods in order to provide an effective reference value for laser cladding coating crack control.

As shown in Table 4, among the six coating crack control methods, the addition of rare earth oxides, the preheating treatment, compound field assistance, new preparation processes, and new structural materials are the most effective for the control of laser melting coating cracks, while post-treatment and laser remelting are generally effective. Numerical analysis can study the melt pool state and thus predict the cracking behavior, where controlling the hard-phase content and optimizing the process parameters are the most widely used. Application of auxiliary fields, numerical analysis, and development of new structural materials and processes are the hotspots of current research with good development prospects.

Table 4. Practical effects, advantages, and disadvantages of the six crack control methods.

Control Methods	Specific Types	Practical Effects	Advantages	Disadvantages
Preferred Cladding Materials	Control of hard-phase contents in the layer	2	Easy to use, wide range of applications	Difficult to eliminate cracks, not applicable without hard phase coating
	Preferred hard-phase particle types	2	Better research prospects	Not applicable without hard-phase coating
	Adding alloying elements	1	Easy to use	Few types of alloy elements and may affect coating properties
	Adding rare earth oxides	0	Wide application range and improving coating properties	High cost, fewer types of rare earth oxides
	Adding transition layer	2	Can reduce coating cracks with high hard-phase content	Small scope of application
Optimization of Cladding Process Parameters	Main process parameters	1	The widest range of applications	Difficult to eliminate cracks in coatings with high hard-phase content
	Other process parameters	2	Better research prospects	High requirements for experimental equipment
Increasing Heat Treatment	Preheat treatment	0	Wide application range	Longer waiting time
	Post-processing	3	Easy to use	The effect is average
	Laser remelting	3	Improving coating properties	Additional costs required
Application of Auxiliary Field	Magnetic field	1	Highly promising research improving coating properties	High requirements for experimental equipment, still in the experimental stage
	Ultrasonic vibrations	1		
	Friction stirring	1		
	Electromagnetic field	1		
	Ultrasonic–electromagnetic field	0	Eliminates cracks in coatings with high hard-phase content	Complex coupling process, extremely demanding equipment
Numerical Analysis	Melt pool and Physical field model	Provide stress distribution diagram	Exploring the melt pool and providing stress distribution diagram	Model complexity and accuracy need to be improved
	Process Parameters and Crack Prediction Model	Predicts optimal processes and cracks	Highly promising research, reducing experiment cost	Longer simulation time and more difficult operation
Other Methods	Novel preparation processes	0	Extremely high research prospect	The research is difficult and still in the exploration stage
	Novel structural materials	0		

Notes: (0) No cracks, (1) almost no cracks, (2) small amounts of cracks, and (3) some cracks remain.

4. Conclusions and Outlook

This paper provides a comprehensive review of crack types, formation mechanisms, and control methods in laser cladding coatings. Additionally, it introduces new approaches involving innovative preparation processes and novel structural materials for crack control in laser cladding coatings.

Cracks in laser cladding coatings primarily arise from residual stresses. The uneven distribution of temperature, stress, and flow fields in the melt pool, along with the temperature gradient and the difference in thermal expansion coefficients and elastic moduli between the molten material and the substrate, make complete elimination of residual stress challenging. Therefore, current research focuses on regulating thermal stress, organizational stress, and restraint stress, reducing individual or interactive stress effects, and inhibiting or eliminating coating cracks during the laser melting process.

To mitigate residual stresses, various control methods are employed, including the selective choice of cladding layer materials, optimization of process parameters, implementation of heat treatment, and application of auxiliary fields. Optimal selection of cladding materials involves choosing hard-phase particles with suitable size, shape, and structure, as well as adding appropriate proportions of alloying elements or rare earth oxides. Process parameter optimization, such as selecting suitable laser cladding parameters and scanning strategies, is crucial. Heat treatment methods such as preheating, slow cooling post-treatment, and laser remelting are employed. The application of auxiliary fields, such as magnetic fields, ultrasonic vibration, electromagnetic fields, friction stirring, and multi-field compounding, is also significant. Furthermore, numerical simulation of the

laser cladding process and the identification and prediction of coating cracks offer valuable perspectives for experimental analysis.

New preparation processes and new structural materials have become a new direction for crack control in laser cladding coatings in recent years. These methods include the use of high-frequency beam oscillation, hybrid laser sources, spot superposition technology, ultra-fine eutectic organization, and core–shell-structured composite powders. These techniques contribute to denser coating structures, reduced residual stresses, and effectively slowing down crack formation tendencies.

However, the current research is mainly focused on the experiments of material proportioning and cladding process parameters as well as the establishment of basic mathematical models. Further control of cracks in laser cladding coatings should be carried out from the following aspects:

(1) Given that the forming mechanism of the melt pool and stress distribution's impact on coating cracks remains unexplored, establishing a comprehensive mathematical model to simulate the entire laser cladding process is necessary. This would provide a theoretical foundation for analyzing crack control in the cladding layer and avoid blind trial and error.

(2) The selection of hard-phase particles in laser cladding coatings lacks sufficient basis, necessitating the development of a standardized table to guide the particle selection process and prevent cracks caused by the variation in actual stress due to different particles.

(3) While the addition of rare earth oxides greatly enhances coating quality, existing additives are limited in variety, expensive, and not suitable for large-scale applications. Thus, new low-cost, high-performance additives need to be developed.

(4) The development of real-time monitoring systems that utilize imaging, temperature sensing, spectral analysis, and sound detection is essential. This would enable real-time regulation of the melt pool temperature and power fluctuations, thereby reducing coating defects and monitoring crack behavior.

(5) As new preparation processes and structural materials significantly improve coating quality and reduce stress, the further exploration and integration of crack control technology with composite preparation processes are crucial to driving the industrial application of laser cladding technology.

References

1. Zhu, L.; Xue, P.; Lan, Q.; Meng, G.; Ren, Y.; Yang, Z.; Xu, P.; Liu, Z. Recent Research and Development Status of Laser Cladding: A Review. *Opt. Laser Technol.* **2021**, *138*, 106915. [CrossRef]
2. He, B.; Zhang, L.; Zhu, Q.; Wang, J.; Yun, X.; Luo, J.; Chen, Z. Effect of Solution Treated 316L Layer Fabricated by Laser Cladding on Wear and Corrosive Wear Resistance. *Opt. Laser Technol.* **2020**, *121*, 105788. [CrossRef]
3. Wang, Q.-Y.; Zhang, Y.-F.; Bai, S.-L.; Liu, Z.-D. Microstructures, Mechanical Properties and Corrosion Resistance of Hastelloy C22 Coating Produced by Laser Cladding. *J. Alloys Compd.* **2013**, *553*, 253–258. [CrossRef]
4. Lu, X.-L.; Liu, X.-B.; Yu, P.-C.; Qiao, S.-J.; Zhai, Y.-J.; Wang, M.-D.; Chen, Y.; Xu, D. Synthesis and Characterization of Ni60-HBN High Temperature Self-Lubricating Anti-Wear Composite Coatings on Ti6Al4V Alloy by Laser Cladding. *Opt. Laser Technol.* **2016**, *78*, 87–94. [CrossRef]
5. Wu, C.L.; Zhang, S.; Zhang, C.H.; Zhang, J.B.; Liu, Y.; Chen, J. Effects of SiC Content on Phase Evolution and Corrosion Behavior of SiC-Reinforced 316L Stainless Steel Matrix Composites by Laser Melting Deposition. *Opt. Laser Technol.* **2019**, *115*, 134–139. [CrossRef]

6. Zhang, P.; Liu, X.; Yan, H. Phase Composition, Microstructure Evolution and Wear Behavior of Ni-Mn-Si Coatings on Copper by Laser Cladding. *Surf. Coat. Technol.* **2017**, *332*, 504–510. [CrossRef]

7. Siddiqui, A.A.; Dubey, A.K. Recent Trends in Laser Cladding and Surface Alloying. *Opt. Laser Technol.* **2021**, *134*, 106619. [CrossRef]

8. Chen, L.; Yu, T.; Chen, X.; Zhao, Y.; Guan, C. Process Optimization, Microstructure and Microhardness of Coaxial Laser Cladding TiC Reinforced Ni-Based Composite Coatings. *Opt. Laser Technol.* **2022**, *152*, 108129. [CrossRef]

9. Lu, J.Z.; Xue, K.N.; Lu, H.F.; Xing, F.; Luo, K.Y. Laser Shock Wave-Induced Wear Property Improvement and Formation Mechanism of Laser Cladding Ni25 Coating on H13 Tool Steel. *J. Mater. Process. Technol.* **2021**, *296*, 117202. [CrossRef]

10. Guo, C.; Chen, J.; Zhou, J.; Zhao, J.; Wang, L.; Yu, Y.; Zhou, H. Effects of WC–Ni Content on Microstructure and Wear Resistance of Laser Cladding Ni-Based Alloys Coating. *Surf. Coat. Technol.* **2012**, *206*, 2064–2071. [CrossRef]

11. Song, J.; Deng, Q.; Chen, C.; Hu, D.; Li, Y. Rebuilding of Metal Components with Laser Cladding Forming. *Appl. Surf. Sci.* **2006**, *252*, 7934–7940. [CrossRef]

12. Lu, M.; McCormick, P.; Zhao, Y.; Fan, Z.; Huang, H. Laser Deposition of Compositionally Graded Titanium Oxide on Ti6Al4V Alloy. *Ceram. Int.* **2018**, *44*, 20851–20861. [CrossRef]

13. Lian, G.; Yao, M.; Zhang, Y.; Huang, X. Analysis and Respond Surface Methodology Modeling on Property and Performance of Two-Dimensional Gradient Material Laser Cladding on Die-Cutting Tool. *Materials* **2018**, *11*, 2052. [CrossRef] [PubMed]

14. Zhang, J.; Song, B.; Wei, Q.; Bourell, D.; Shi, Y. A Review of Selective Laser Melting of Aluminum Alloys: Processing, Microstructure, Property and Developing Trends. *J. Mater. Sci. Technol.* **2019**, *35*, 270–284. [CrossRef]

15. Galy, C.; Le Guen, E.; Lacoste, E.; Arvieu, C. Main Defects Observed in Aluminum Alloy Parts Produced by SLM: From Causes to Consequences. *Addit. Manuf.* **2018**, *22*, 165–175. [CrossRef]

16. Quazi, M.M.; Fazal, M.A.; Haseeb, A.S.M.A.; Yusof, F.; Masjuki, H.H.; Arslan, A. Effect of Rare Earth Elements and Their Oxides on Tribo-Mechanical Performance of Laser Claddings: A Review. *J. Rare Earths* **2016**, *34*, 549–564. [CrossRef]

17. Wang, X.; Lei, L.; Yu, H. A Review on Microstructural Features and Mechanical Properties of Wheels/Rails Cladded by Laser Cladding. *Micromachines* **2021**, *12*, 152. [CrossRef] [PubMed]

18. Hu, Y.; Cong, W. A Review on Laser Deposition-Additive Manufacturing of Ceramics and Ceramic Reinforced Metal Matrix Composites. *Ceram. Int.* **2018**, *44*, 20599–20612. [CrossRef]

19. Fang, Z.-C.; Wu, Z.-L.; Huang, C.-G.; Wu, C.-W. Review on Residual Stress in Selective Laser Melting Additive Manufacturing of Alloy Parts. *Opt. Laser Technol.* **2020**, *129*, 106283. [CrossRef]

20. Sanaei, N.; Fatemi, A. Defects in Additive Manufactured Metals and Their Effect on Fatigue Performance: A State-of-the-Art Review. *Prog. Mater. Sci.* **2021**, *117*, 100724. [CrossRef]

21. Cheng, J.; Xing, Y.; Dong, E.; Zhao, L.; Liu, H.; Chang, T.; Chen, M.; Wang, J.; Lu, J.; Wan, J. An Overview of Laser Metal Deposition for Cladding: Defect Formation Mechanisms, Defect Suppression Methods and Performance Improvements of Laser-Cladded Layers. *Materials* **2022**, *15*, 5522. [CrossRef] [PubMed]

22. Wang, F.; Mao, H.; Zhang, D.; Zhao, X.; Shen, Y. Online Study of Cracks during Laser Cladding Process Based on Acoustic Emission Technique and Finite Element Analysis. *Appl. Surf. Sci.* **2008**, *255*, 3267–3275. [CrossRef]

23. Wang, D.; Liang, E.; Chao, M.; Yuan, B. Investigation on the Microstructure and Cracking Susceptibility of Laser-Clad V_2O_5/NiCrBSiC Alloy Coatings. *Surf. Coat. Technol.* **2008**, *202*, 1371–1378. [CrossRef]

24. Cloots, M.; Uggowitzer, P.J.; Wegener, K. Investigations on the Microstructure and Crack Formation of IN738LC Samples Processed by Selective Laser Melting Using Gaussian and Doughnut Profiles. *Mater. Des.* **2016**, *89*, 770–784. [CrossRef]

25. Eo, D.-R.; Chung, S.-G.; Yang, J.; Cho, W.T.; Park, S.-H.; Cho, J.-W. Surface Modification of High-Mn Steel via Laser-DED: Microstructural Characterization and Hot Crack Susceptibility of Clad Layer. *Mater. Des.* **2022**, *223*, 111188. [CrossRef]

26. Alizadeh-Sh, M.; Marashi, S.P.H.; Ranjbarnodeh, E.; Shoja-Razavi, R. Laser Cladding of Inconel 718 Powder on a Non-Weldable Substrate: Clad Bead Geometry-Solidification Cracking Relationship. *J. Manuf. Process.* **2020**, *56*, 54–62. [CrossRef]

27. Shankar, V.; Gill, T.P.S.; Mannan, S.L.; Terrance, A.L.E.; Sundaresan, S. Relation between Microstructure, Composition, and Hot Cracking in Ti-Stabilized Austenitic Stainless Steel Weldments. *Metall. Mater. Trans. A* **2000**, *31*, 3109–3122. [CrossRef]

28. Chen, Y.; Lu, F.; Zhang, K.; Nie, P.; Elmi Hosseini, S.R.; Feng, K.; Li, Z. Dendritic Microstructure and Hot Cracking of Laser Additive Manufactured Inconel 718 under Improved Base Cooling. *J. Alloys Compd.* **2016**, *670*, 312–321. [CrossRef]

29. Ebrahimzadeh, H.; Farhangi, H.; Mousavi, S.A.A.A. Hot Cracking in Autogenous Welding of 6061-T6 Aluminum Alloy by Rectangular Pulsed Nd: YAG Laser Beam. *Weld. World* **2020**, *64*, 1077–1088. [CrossRef]

30. Zenitani, S.; Hayakawa, N.; Yamamoto, J.; Hiraoka, K.; Morikage, Y.; Kubo, T.; Yasuda, K.; Amano, K. Development of New Low Transformation Temperature Welding Consumable to Prevent Cold Cracking in High Strength Steel Welds. *Sci. Technol. Weld. Join.* **2007**, *12*, 516–522. [CrossRef]

31. Hu, L.H.; Huang, J.; Li, Z.G.; Wu, Y.X. Effects of Preheating Temperature on Cold Cracks, Microstructures and Properties of High Power Laser Hybrid Welded 10Ni3CrMoV Steel. *Mater. Des.* **2011**, *32*, 1931–1939. [CrossRef]

32. Boes, J.; Röttger, A.; Theisen, W. Processing of X65MoCrWV3-2 Cold Work Tool Steel by Laser Powder Bed Fusion. *Steel Res. Int.* **2020**, *91*, 1900445. [CrossRef]

33. Li, K.; Wang, X.; Brodusch, N.; Tu, G. Mitigating Cracking in Laser Powder Bed Fusion of Ti-48Al-2Cr-2Nb via Introducing Massive β Phase. *Mater. Charact.* **2023**, *196*, 112558. [CrossRef]

34. Sadhu, A.; Choudhary, A.; Sarkar, S.; Nair, A.M.; Nayak, P.; Pawar, S.D.; Muvvala, G.; Pal, S.K.; Nath, A.K. A Study on the Influence of Substrate Pre-Heating on Mitigation of Cracks in Direct Metal Laser Deposition of NiCrSiBC-60%WC Ceramic Coating on Inconel 718. *Surf. Coat. Technol.* **2020**, *389*, 125646. [CrossRef]

35. Liu, S.; Sun, Y.; Zhai, P.; Fan, P.; Zhang, Y.; Li, M.; Fang, J.; Wu, R.; Cai, Z. Microstructure and Properties of Nickel-Based Gradient Coatings Prepared Using Cold Spraying Combined with Laser Cladding Methods. *Materials* **2023**, *16*, 1627. [CrossRef]

36. Dmitrieva, A.; Klimova-Korsmik, O.; Gushchina, M.; Korsmik, R.; Zadykyan, G.; Tukov, S. Effect of the Laser Cladding Parameters on the Crack Formation and Microstructure during Nickel Superalloy Gas Turbine Engines Repair. *Metals* **2023**, *13*, 393. [CrossRef]

37. Zhang, Z.; Zhao, Y.; Chen, Y.; Su, Z.; Shan, J.; Wu, A.; Sato, Y.S.; Gu, H.; Tang, X. The Role of the Pulsed-Wave Laser Characteristics on Restraining Hot Cracking in Laser Cladding Non-Weldable Nickel-Based Superalloy. *Mater. Des.* **2021**, *198*, 109346. [CrossRef]

38. Meng, L.; Sheng, P.; Zeng, X. Comparative Studies on the Ni60 Coatings Deposited by Conventional and Induction Heating Assisted Extreme-High-Speed Laser Cladding Technology: Formability, Microstructure and Hardness. *J. Mater. Res. Technol.* **2022**, *16*, 1732–1746. [CrossRef]

39. Ma, Q.; Lu, B.; Zhang, Y.; Wang, Y.; Yan, X.; Liu, M.; Zhao, G. Crack-Free 60 Wt% WC Reinforced FeCoNiCr High-Entropy Alloy Composite Coating Fabricated by Laser Cladding. *Mater. Lett.* **2022**, *324*, 132667. [CrossRef]

40. Wang, K.; Liu, B.; Wang, Q.; Bao, R. Macrostructures and Mechanical Properties in Laser Melting Deposited Titanium Alloy Plate at Different Thickness Positions. *Mater. Sci. Eng. A* **2022**, *832*, 142433. [CrossRef]

41. Wang, K.; Bao, R.; Liu, D.; Yan, C. Plastic Anisotropy of Laser Melting Deposited Ti–5Al–5Mo–5V–1Cr–1Fe Titanium Alloy. *Mater. Sci. Eng. A* **2019**, *746*, 276–289. [CrossRef]

42. Mishra, R.S.; Ma, Z.Y. Friction Stir Welding and Processing. *Mater. Sci. Eng. R Rep.* **2005**, *50*, 1–78. [CrossRef]

43. Wu, P.; Du, H.M.; Chen, X.L.; Li, Z.Q.; Bai, H.L.; Jiang, E.Y. Influence of WC Particle Behavior on the Wear Resistance Properties of Ni–WC Composite Coatings. *Wear* **2004**, *257*, 142–147. [CrossRef]

44. Bussu, G.; Irving, P. The Role of Residual Stress and Heat Affected Zone Properties on Fatigue Crack Propagation in Friction Stir Welded 2024-T351 Aluminium Joints. *Int. J. Fatigue* **2003**, *25*, 77–88. [CrossRef]

45. Zhang, Z.; Kovacevic, R. A Thermo-Mechanical Model for Simulating the Temperature and Stress Distribution during Laser Cladding Process. *Int. J. Adv. Manuf. Technol.* **2019**, *102*, 457–472. [CrossRef]

46. Zhou, S.; Zeng, X.; Hu, Q.; Huang, Y. Analysis of Crack Behavior for Ni-Based WC Composite Coatings by Laser Cladding and Crack-Free Realization. *Appl. Surf. Sci.* **2008**, *255*, 1646–1653. [CrossRef]

47. Ignat, S.; Sallamand, P.; Nichici, A.; Vannes, B.; Grevey, D.; Cicală, E. MoSi$_2$ Laser Cladding—Elaboration, Characterisation and Addition of Non-Stabilized ZrO$_2$ Powder Particles. *Intermetallics* **2003**, *11*, 931–938. [CrossRef]

48. Shah, K.; Khurshid, H.; ul Haq, I.; Anwar, S.; Shah, S.A. Numerical Modelling of Pulsed and Continuous Wave Direct Laser Deposition of Ti-6Al-4V and Inconel 718. *Int. J. Adv. Manuf. Technol.* **2018**, *95*, 847–860. [CrossRef]

49. Sun, S.; Fu, H.; Chen, S.; Ping, X.; Wang, K.; Guo, X.; Lin, J.; Lei, Y. A Numerical-Experimental Investigation of Heat Distribution, Stress Field and Crack Susceptibility in Ni60A Coatings. *Opt. Laser Technol.* **2019**, *117*, 175–185. [CrossRef]

50. Ramakrishnan, A.; Dinda, G.P. Direct Laser Metal Deposition of Inconel 738. *Mater. Sci. Eng. A* **2019**, *740–741*, 1–13. [CrossRef]

51. Brauner, N.; Shacham, M. Statistical Analysis of Linear and Nonlinear Correlation of the Arrhenius Equation Constants. *Chem. Eng. Process. Process Intensif.* **1997**, *36*, 243–249. [CrossRef]

52. Zhou, Z.; Di, X.; Li, C.; Wu, S. Effect of Restraint Stress on Martensite Transformation in Low Transformation Temperature Weld Metal. *J. Mater. Sci.* **2020**, *55*, 2202–2214. [CrossRef]

53. Bendeich, P.; Alam, N.; Brandt, M.; Carr, D.; Short, K.; Blevins, R.; Curfs, C.; Kirstein, O.; Atkinson, G.; Holden, T.; et al. Residual Stress Measurements in Laser Clad Repaired Low Pressure Turbine Blades for the Power Industry. *Mater. Sci. Eng. A* **2006**, *437*, 70–74. [CrossRef]

54. Kirchlechner, C.; Martinschitz, K.J.; Daniel, R.; Klaus, M.; Genzel, C.; Mitterer, C.; Keckes, J. Residual Stresses and Thermal Fatigue in CrN Hard Coatings Characterized by High-Temperature Synchrotron X-Ray Diffraction. *Thin Solid Films* **2010**, *518*, 2090–2096. [CrossRef]

55. Dixneit, J.; Kromm, A.; Hannemann, A.; Friedersdorf, P.; Kannengiesser, T.; Gibmeier, J. In-Situ Load Analysis in Multi-Run Welding Using LTT Filler Materials. *Weld. World* **2016**, *60*, 1159–1168. [CrossRef]

56. Yu, T.; Deng, Q.; Dong, G.; Yang, J. Effects of Ta on Microstructure and Microhardness of Ni Based Laser Clad Coating. *Appl. Surf. Sci.* **2011**, *257*, 5098–5103. [CrossRef]

57. Zhang, S.H.; Li, M.X.; Cho, T.Y.; Yoon, J.H.; Lee, C.G.; He, Y.Z. Laser Clad Ni-Base Alloy Added Nano- and Micron-Size CeO$_2$ Composites. *Opt. Laser Technol.* **2008**, *40*, 716–722. [CrossRef]

58. Zheng, B.J.; Chen, X.M.; Lian, J.S. Microstructure and Wear Property of Laser Cladding Al+SiC Powders on AZ91D Magnesium Alloy. *Opt. Lasers Eng.* **2010**, *48*, 526–532. [CrossRef]

59. Xu, G.; Kutsuna, M.; Liu, Z.; Zhang, H. Characteristics of Ni-Based Coating Layer Formed by Laser and Plasma Cladding Processes. *Mater. Sci. Eng. A* **2006**, *417*, 63–72. [CrossRef]

60. Huang, L.; Zhou, J.; Xu, J.; Huo, K.; He, W.; Meng, X.; Huang, S. Microstructure and Wear Resistance of Electromagnetic Field Assisted Multi-Layer Laser Clad Fe901 Coating. *Surf. Coat. Technol.* **2020**, *395*, 125876. [CrossRef]

61. Li, X.P.; Roberts, M.; Liu, Y.J.; Kang, C.W.; Huang, H.; Sercombe, T.B. Effect of Substrate Temperature on the Interface Bond between Support and Substrate during Selective Laser Melting of Al–Ni–Y–Co–La Metallic Glass. *Mater. Des. (1980–2015)* **2015**, *65*, 1–6. [CrossRef]

62. Gan, Z.; Yu, G.; He, X.; Li, S. Surface-Active Element Transport and Its Effect on Liquid Metal Flow in Laser-Assisted Additive Manufacturing. *Int. Commun. Heat Mass Transf.* **2017**, *86*, 206–214. [CrossRef]

63. Gao, Z.; Wang, L.; Wang, Y.; Lyu, F.; Zhan, X. Crack Defects and Formation Mechanism of FeCoCrNi High Entropy Alloy Coating on TC4 Titanium Alloy Prepared by Laser Cladding. *J. Alloys Compd.* **2022**, *903*, 163905. [CrossRef]

64. Ning, Z.; Li, T.; Hui, G.; Mengqi, Z. Effect of Ultra-Fine WC Particles on Microstructural Evolution and Wear Behavior of Ni-Based Nano-CeO2 Coatings Produced by Laser. *Rare Met. Mater. Eng.* **2018**, *47*, 20–25. [CrossRef]

65. Shen, X.; Peng, H.; Xue, Y.; Wang, B.; Su, G.; Zhu, J.; Li, A. Microstructure and Properties of WC/Ni-Based Laser-Clad Coatings with Different WC Content Values. *Materials* **2022**, *15*, 6309. [CrossRef]

66. Shen, X.; He, X.; Gao, L.; Su, G.; Xu, C.; Xu, N. Study on Crack Behavior of Laser Cladding Ceramic-Metal Composite Coating with High Content of WC. *Ceram. Int.* **2022**, *48*, 17460–17470. [CrossRef]

67. Liu, D.; Zhang, S.Q.; Li, A.; Wang, H.M. Microstructure and Tensile Properties of Laser Melting Deposited TiC/TA15 Titanium Matrix Composites. *J. Alloys Compd.* **2009**, *485*, 156–162. [CrossRef]

68. Zhang, P.; Pang, Y.; Yu, M. Effects of WC Particle Types on the Microstructures and Properties of WC-Reinforced Ni60 Composite Coatings Produced by Laser Cladding. *Metals* **2019**, *9*, 583. [CrossRef]

69. Sun, Z.; Ma, Y.; Ponge, D.; Zaefferer, S.; Jägle, E.A.; Gault, B.; Rollett, A.D.; Raabe, D. Thermodynamics-Guided Alloy and Process Design for Additive Manufacturing. *Nat. Commun.* **2022**, *13*, 4361. [CrossRef]

70. Chen, H.; Xu, C.; Chen, J.; Zhao, H.; Zhang, L.; Wang, Z. Microstructure and Phase Transformation of WC/Ni60B Laser Cladding Coatings during Dry Sliding Wear. *Wear* **2008**, *264*, 487–493. [CrossRef]

71. Paul, C.P.; Toyserkani, E.; Khajepour, A.; Corbin, S. Cladding of WC–12 Co on Low Carbon Steel Using a Pulsed Nd:YAG Laser. *Mater. Sci. Eng. A* **2007**, *464*, 170–176. [CrossRef]

72. Wang, K.L.; Zhang, Q.B.; Sun, M.L.; Wei, X.G. Microstructural Characteristics of Laser Clad Coatings with Rare Earth Metal Elements. *J. Mater. Process. Technol.* **2003**, *139*, 448–452. [CrossRef]

73. He, X.; Song, R.G.; Kong, D.J. Effects of TiC on the Microstructure and Properties of TiC/TiAl Composite Coating Prepared by Laser Cladding. *Opt. Laser Technol.* **2019**, *112*, 339–348. [CrossRef]

74. Wang, H.; Zuo, D.; Sun, Y.; Xu, F.; Zhang, D. Microstructure of Nanometer Al2O3 Dispersion Strengthened Ni-Based High-Temperature Protective Coatings by Laser Cladding. *Trans. Nonferrous Met. Soc. China* **2009**, *19*, 586–591. [CrossRef]

75. Li, X.; Yang, X.; Yi, D.; Liu, B.; Zhu, J.; Li, J.; Gao, C.; Wang, L. Effects of NbC Content on Microstructural Evolution and Mechanical Properties of Laser Cladded Fe50Mn30Co10Cr10-XNbC Composite Coatings. *Intermetallics* **2021**, *138*, 107309. [CrossRef]

76. Zhang, J.; Lei, J.; Gu, Z.; Tantai, F.; Tian, H.; Han, J.; Fang, Y. Effect of WC-12Co Content on Wear and Electrochemical Corrosion Properties of Ni-Cu/WC-12Co Composite Coatings Deposited by Laser Cladding. *Surf. Coat. Technol.* **2020**, *393*, 125807. [CrossRef]

77. Mazaheri Tehrani, H.; Shoja-Razavi, R.; Erfanmanesh, M.; Hashemi, S.H.; Barekat, M. Evaluation of the Mechanical Properties of WC-Ni Composite Coating on an AISI 321 Steel Substrate. *Opt. Laser Technol.* **2020**, *127*, 106138. [CrossRef]

78. Dai, Q.-L.; Luo, C.; You, F. Crack Restraining Methods and Their Effects on the Microstructures and Properties of Laser Cladded WC/Fe Coatings. *Materials* **2018**, *11*, 2541. [CrossRef]

79. Qi, K.; Yang, Y.; Liang, W.; Jin, K.; Xiong, L. Influence of the Anomalous Elastic Modulus on the Crack Sensitivity and Wear Properties of Laser Cladding under the Effects of a Magnetic Field and Cr Addition. *Surf. Coat. Technol.* **2021**, *423*, 127575. [CrossRef]

80. Sun, S.; Fu, H.; Ping, X.; Guo, X.; Lin, J.; Lei, Y.; Wu, W.; Zhou, J. Effect of CeO2 Addition on Microstructure and Mechanical Properties of In-Situ (Ti, Nb) C/Ni Coating. *Surf. Coat. Technol.* **2019**, *359*, 300–313. [CrossRef]

81. Shu, D.; Dai, S.; Wang, G.; Si, W.; Xiao, P.; Cui, X.; Chen, X. Influence of CeO2 Content on WC Morphology and Mechanical Properties of WC/Ni Matrix Composites Coating Prepared by Laser in-Situ Synthesis Method. *J. Mater. Res. Technol.* **2020**, *9*, 11111–11120. [CrossRef]

82. Zhang, M.; Wang, X.H.; Qu, K.L.; Liu, S.S. Effect of Rare Earth Oxide on Microstructure and High Temperature Oxidation Properties of Laser Cladding Coatings on 5CrNiMo Die Steel Substrate. *Opt. Laser Technol.* **2019**, *119*, 105597. [CrossRef]

83. Li, J.; Luo, X.; Li, G.J. Effect of Y2O3 on the Sliding Wear Resistance of TiB/TiC-Reinforced Composite Coatings Fabricated by Laser Cladding. *Wear* **2014**, *310*, 72–82. [CrossRef]

84. Li, M.; Han, B.; Wang, Y.; Pu, K. Effects of La2O3 on the Microstructure and Property of Laser Cladding Ni-Based Ceramic Coating. *Optik* **2017**, *130*, 1032–1037. [CrossRef]

85. Farahmand, P.; Liu, S.; Zhang, Z.; Kovacevic, R. Laser Cladding Assisted by Induction Heating of Ni–WC Composite Enhanced by Nano-WC and La2O3. *Ceram. Int.* **2014**, *40*, 15421–15438. [CrossRef]

86. Tian, Y.S.; Chen, C.Z.; Chen, L.X.; Huo, Q.H. Effect of RE Oxides on the Microstructure of the Coatings Fabricated on Titanium Alloys by Laser Alloying Technique. *Scr. Mater.* **2006**, *54*, 847–852. [CrossRef]

87. Zhang, Z.; Yang, F.; Zhang, H.; Zhang, T.; Wang, H.; Xu, Y.; Ma, Q. Influence of CeO2 Addition on Forming Quality and Microstructure of TiC -Reinforced CrTi4-Based Laser Cladding Composite Coating. *Mater. Charact.* **2021**, *171*, 110732. [CrossRef]

88. Yuling, G.; Meiping, W.; Xiaojin, M.; Chen, C. Effect of CeO2 on Crack Sensitivity and Tribological Properties of Ni60A Coatings Prepared by Laser Cladding. *Adv. Mech. Eng.* **2021**, *13*, 168781402110131. [CrossRef]

89. Wang, C.; Gao, Y.; Zeng, Z.; Fu, Y. Effect of Rare-Earth on Friction and Wear Properties of Laser Cladding Ni-Based Coatings on 6063Al. *J. Alloys Compd.* **2017**, *727*, 278–285. [CrossRef]

90. Tey, C.F.; Tan, X.; Sing, S.L.; Yeong, W.Y. Additive Manufacturing of Multiple Materials by Selective Laser Melting: Ti-Alloy to Stainless Steel via a Cu-Alloy Interlayer. *Addit. Manuf.* **2020**, *31*, 100970. [CrossRef]

91. Zhang, Y.; Wei, Z.; Shi, L.; Xi, M. Characterization of Laser Powder Deposited Ti–TiC Composites and Functional Gradient Materials. *J. Mater. Process. Technol.* **2008**, *206*, 438–444. [CrossRef]

92. Mahamood, R.M.; Akinlabi, E.T. Laser Metal Deposition of Functionally Graded Ti6Al4V/TiC. *Mater. Des.* **2015**, *84*, 402–410. [CrossRef]

93. Cao, S.; Liang, J.; Wang, L.; Zhou, J. Effects of NiCr Intermediate Layer on Microstructure and Tribological Property of Laser Cladding Cr$_3$C$_2$ Reinforced Ni60A-Ag Composite Coating on Copper Alloy. *Opt. Laser Technol.* **2021**, *142*, 106963. [CrossRef]

94. Cai, Y.; Sun, D.; Cui, Y.; Manladan, S.M.; Wang, T.; Shan, M.; Han, J. Effect of CoCrFeMnNi Transition Cladding Layer on Crack Resistance of CoCrFeMnNi + x(TiC) Composite Cladding Layer. *Mater. Lett.* **2021**, *304*, 130700. [CrossRef]

95. Thawari, N.; Gullipalli, C.; Katiyar, J.K.; Gupta, T.V.K. Influence of Buffer Layer on Surface and Tribomechanical Properties of Laser Cladded Stellite 6. *Mater. Sci. Eng. B* **2021**, *263*, 114799. [CrossRef]

96. Wang, Q.; Li, Q.; Zhang, L.; Chen, D.X.; Jin, H.; Li, J.D.; Zhang, J.W.; Ban, C.Y. Microstructure and Properties of Ni-WC Gradient Composite Coating Prepared by Laser Cladding. *Ceram. Int.* **2022**, *48*, 7905–7917. [CrossRef]

97. Li, L.; Wang, J.; Lin, P.; Liu, H. Microstructure and Mechanical Properties of Functionally Graded TiCp/Ti6Al4V Composite Fabricated by Laser Melting Deposition. *Ceram. Int.* **2017**, *43*, 16638–16651. [CrossRef]

98. Lee, Y.; Nordin, M.; Babu, S.S.; Farson, D.F. Effect of Fluid Convection on Dendrite Arm Spacing in Laser Deposition. *Metall. Mater. Trans. B* **2014**, *45*, 1520–1529. [CrossRef]

99. Fu, F.; Zhang, Y.; Chang, G.; Dai, J. Analysis on the Physical Mechanism of Laser Cladding Crack and Its Influence Factors. *Optik* **2016**, *127*, 200–202. [CrossRef]

100. El-Labban, H.F.; Mahmoud, E.R.I.; Algahtani, A. Microstructure, Wear, and Corrosion Characteristics of TiC-Laser Surface Cladding on Low-Carbon Steel. *Metall. Mater. Trans. B* **2016**, *47*, 974–982. [CrossRef]

101. Valsecchi, B.; Previtali, B.; Vedani, M.; Vimercati, G. Fiber Laser Cladding with High Content of WC-Co Based Powder. *Int. J. Mater.* **2010**, *3*, 1127–1130. [CrossRef]

102. Song, M.; Wu, L.; Liu, J.; Hu, Y. Effects of Laser Cladding on Crack Resistance Improvement for Aluminum Alloy Used in Aircraft Skin. *Opt. Laser Technol.* **2021**, *133*, 106531. [CrossRef]

103. Xiong, Z.; Chen, G.; Zeng, X. Effects of Process Variables on Interfacial Quality of Laser Cladding on Aeroengine Blade Material GH4133. *J. Mater. Process. Technol.* **2009**, *209*, 930–936. [CrossRef]

104. Baldridge, T.; Poling, G.; Foroozmehr, E.; Kovacevic, R.; Metz, T.; Kadekar, V.; Gupta, M.C. Laser Cladding of Inconel 690 on Inconel 600 Superalloy for Corrosion Protection in Nuclear Applications. *Opt. Lasers Eng.* **2013**, *51*, 180–184. [CrossRef]

105. Yu, J.; Sun, W.; Huang, H.; Wang, W.; Wang, Y.; Hu, Y. Crack Sensitivity Control of Nickel-Based Laser Coating Based on Genetic Algorithm and Neural Network. *Coatings* **2019**, *9*, 728. [CrossRef]

106. Hu, G.; Yang, Y.; Qi, K.; Lu, X.; Li, J. Investigation of the Microstructure and Properties of NiCrBSi Coating Obtained by Laser Cladding with Different Process Parameters. *Trans. Indian Inst. Met.* **2020**, *73*, 2623–2634. [CrossRef]

107. Majumdar, J.D.; Rittinghaus, S.K.; Wissenbach, K.; Höche, D.; Blawert, C.; Weisheit, A. Direct Laser Cladding of the Silicide Dispersed Titanium Aluminide (Ti45Al5Nb0.5Si) Composites. *Opt. Laser Technol.* **2018**, *106*, 182–190. [CrossRef]

108. Desale, G.R.; Paul, C.P.; Gandhi, B.K.; Jain, S.C. Erosion Wear Behavior of Laser Clad Surfaces of Low Carbon Austenitic Steel. *Wear* **2009**, *266*, 975–987. [CrossRef]

109. Saboori, A.; Gallo, D.; Biamino, S.; Fino, P.; Lombardi, M. An Overview of Additive Manufacturing of Titanium Components by Directed Energy Deposition: Microstructure and Mechanical Properties. *Appl. Sci.* **2017**, *7*, 883. [CrossRef]

110. Beuth, J.; Klingbeil, N. The Role of Process Variables in Laser-Based Direct Metal Solid Freeform Fabrication. *JOM* **2001**, *53*, 36–39. [CrossRef]

111. Javid, Y. Multi-Response Optimization in Laser Cladding Process of WC Powder on Inconel 718. *CIRP J. Manuf. Sci. Technol.* **2020**, *31*, 406–417. [CrossRef]

112. Khorram, A.; Davoodi Jamaloei, A.; Sepehrnia, R. Analysis of Solidification Crack Behavior for Amdry 997 Coating on Inconel 713 LC Superalloy by Laser Cladding Process. *Optik* **2022**, *264*, 169407. [CrossRef]

113. Shi, B.; Mu, X.; Zhan, H.; Deng, L.; Li, T.; Zhang, H. Crack Behavior of Ni60A Coating Prepared by Laser Cladding on a Tilted Substrate. *Coatings* **2022**, *12*, 966. [CrossRef]

114. Yamaguchi, T.; Hagino, H. Effects of the Ambient Oxygen Concentration on WC-12Co Cermet Coatings Fabricated by Laser Cladding. *Opt. Laser Technol.* **2021**, *139*, 106922. [CrossRef]

115. Ding, C.; Cui, X.; Jiao, J.; Zhu, P. Effects of Substrate Preheating Temperatures on the Microstructure, Properties, and Residual Stress of 12CrNi2 Prepared by Laser Cladding Deposition Technique. *Materials* **2018**, *11*, 2401. [CrossRef]

116. Bidron, G.; Doghri, A.; Malot, T.; Fournier-Dit-Chabert, F.; Thomas, M.; Peyre, P. Reduction of the Hot Cracking Sensitivity of CM-247LC Superalloy Processed by Laser Cladding Using Induction Preheating. *J. Mater. Process. Technol.* **2020**, *277*, 116461. [CrossRef]

117. Zhou, S.; Huang, Y.; Zeng, X.; Hu, Q. Microstructure Characteristics of Ni-Based WC Composite Coatings by Laser Induction Hybrid Rapid Cladding. *Mater. Sci. Eng. A* **2008**, *480*, 564–572. [CrossRef]

118. Li, G.J.; Li, J.; Luo, X. Effects of Post-Heat Treatment on Microstructure and Properties of Laser Cladded Composite Coatings on Titanium Alloy Substrate. *Opt. Laser Technol.* **2015**, *65*, 66–75. [CrossRef]

119. Chen, J.-Y.; Conlon, K.; Xue, L.; Rogge, R. Experimental Study of Residual Stresses in Laser Clad AISI P20 Tool Steel on Pre-Hardened Wrought P20 Substrate. *Mater. Sci. Eng. A* **2010**, *527*, 7265–7273. [CrossRef]
120. Chen, J.; Wang, S.-H.; Xue, L. On the Development of Microstructures and Residual Stresses during Laser Cladding and Post-Heat Treatments. *J. Mater. Sci.* **2012**, *47*, 779–792. [CrossRef]
121. Telasang, G.; Dutta Majumdar, J.; Wasekar, N.; Padmanabham, G.; Manna, I. Microstructure and Mechanical Properties of Laser Clad and Post-Cladding Tempered AISI H13 Tool Steel. *Metall. Mater. Trans. A* **2015**, *46*, 2309–2321. [CrossRef]
122. Wang, H.; Cheng, Y.; Yang, J.; Wang, Q. Influence of Laser Remelting on Organization, Mechanical Properties and Corrosion Resistance of Fe-Based Amorphous Composite Coating. *Surf. Coat. Technol.* **2021**, *414*, 127081. [CrossRef]
123. Lu, Y.; Huang, G.; Wang, Y.; Li, H.; Qin, Z.; Lu, X. Crack-Free Fe-Based Amorphous Coating Synthesized by Laser Cladding. *Mater. Lett.* **2018**, *210*, 46–50. [CrossRef]
124. Zhai, L.L.; Zhang, J.W.; Ban, C.Y. Influence on the Microstructure of Laser Cladding NiCrBSi Coatings with Electromagnetic Compound Field. *SSP* **2019**, *295*, 15–20. [CrossRef]
125. Xie, S.; Li, R.; Yuan, T.; Chen, C.; Zhou, K.; Song, B.; Shi, Y. Laser Cladding Assisted by Friction Stir Processing for Preparation of Deformed Crack-Free Ni-Cr-Fe Coating with Nanostructure. *Opt. Laser Technol.* **2018**, *99*, 374–381. [CrossRef]
126. Li, M.; Han, B.; Wang, Y.; Song, L.; Guo, L. Investigation on Laser Cladding High-Hardness Nano-Ceramic Coating Assisted by Ultrasonic Vibration Processing. *Optik* **2016**, *127*, 4596–4600. [CrossRef]
127. Qi, K.; Yang, Y.; Sun, R.; Hu, G.; Lu, X.; Li, J.; Liang, W.; Jin, K.; Xiong, L. Effect of Magnetic Field on Crack Control of Co-Based Alloy Laser Cladding. *Opt. Laser Technol.* **2021**, *141*, 107129. [CrossRef]
128. Han, X.; Li, C.; Yang, Y.; Gao, X.; Gao, H. Experimental Research on the Influence of Ultrasonic Vibrations on the Laser Cladding Process of a Disc Laser. *Surf. Coat. Technol.* **2021**, *406*, 126750. [CrossRef]
129. Wang, Q.; Chen, F.Q.; Li, Q.; Zhang, L.; Jin, H.; Zhang, J.W. Microstructure and Properties of Ni60 Alloy Coating Prepared by Electromagnetic Compound Field Assisted Laser Cladding. *Mater. Chem. Phys.* **2022**, *291*, 126678. [CrossRef]
130. Hu, G.; Yang, Y.; Sun, R.; Qi, K.; Lu, X.; Li, J. Microstructure and Properties of Laser Cladding NiCrBSi Coating Assisted by Electromagnetic-Ultrasonic Compound Field. *Surf. Coat. Technol.* **2020**, *404*, 126469. [CrossRef]
131. Wang, Q.; Zhai, L.L.; Zhang, L.; Zhang, J.W.; Ban, C.Y. Effect of Steady Magnetic Field on Microstructure and Properties of Laser Cladding Ni-Based Alloy Coating. *J. Mater. Res. Technol.* **2022**, *17*, 2145–2157. [CrossRef]
132. Zhang, M.; Zhao, G.L.; Wang, X.H.; Liu, S.S.; Ying, W.L. Microstructure Evolution and Properties of In-Situ Ceramic Particles Reinforced Fe-Based Composite Coating Produced by Ultrasonic Vibration Assisted Laser Cladding Processing. *Surf. Coat. Technol.* **2020**, *403*, 126445. [CrossRef]
133. Niu, P.; Li, R.; Yuan, T.; Wang, M.; Xie, S.; Wu, H. Laser Solid Forming Assisted by Friction Stir Processing for Preparation of Ni–16Cr–8Fe Alloys: Crack Repairing and Grain Refinement. *J. Mater. Res.* **2018**, *33*, 3521–3529. [CrossRef]
134. Aliabadi, M.; Khodabakhshi, F.; Soltani, R.; Gerlich, A.P. Modification of Flame-Sprayed NiCrBSi Alloy Wear-Resistant Coating by Friction Stir Processing and Furnace Re-Melting Treatments. *Surf. Coat. Technol.* **2023**, *455*, 129236. [CrossRef]
135. Zhang, T.; Zhou, J.; Wang, J.; Meng, X.; Li, P.; Huang, S.; Zhu, H. Effect of Hybrid Ultrasonic-Electromagnetic Field on Cracks and Microstructure of Inconel 718/60%WC Composites Coating Fabricated by Laser Cladding. *Ceram. Int.* **2022**, *48*, 33901–33913. [CrossRef]
136. Wang, L.; Yao, J.; Hu, Y.; Zhang, Q.; Sun, Z.; Liu, R. Influence of Electric-Magnetic Compound Field on the WC Particles Distribution in Laser Melt Injection. *Surf. Coat. Technol.* **2017**, *315*, 32–43. [CrossRef]
137. Kumar, A.; Roy, S. Effect of Three-Dimensional Melt Pool Convection on Process Characteristics during Laser Cladding. *Comput. Mater. Sci.* **2009**, *46*, 495–506. [CrossRef]
138. Chew, Y.; Pang, J.H.L.; Bi, G.; Song, B. Thermo-Mechanical Model for Simulating Laser Cladding Induced Residual Stresses with Single and Multiple Clad Beads. *J. Mater. Process. Technol.* **2015**, *224*, 89–101. [CrossRef]
139. Aucott, L.; Dong, H.; Mirihanage, W.; Atwood, R.; Kidess, A.; Gao, S.; Wen, S.; Marsden, J.; Feng, S.; Tong, M.; et al. Revealing Internal Flow Behaviour in Arc Welding and Additive Manufacturing of Metals. *Nat. Commun.* **2018**, *9*, 5414. [CrossRef]
140. Yao, Z.; Chen, J.; Qian, H.; Nie, Y.; Zhang, Q.; Yao, J. Microstructure and Tensile Property of Laser Cladding Assisted with Multidimensional High-Frequency Vibration. *Materials* **2022**, *15*, 4295. [CrossRef]
141. Tian, J.; Xu, P.; Liu, Q. Effects of Stress-Induced Solid Phase Transformations on Residual Stress in Laser Cladding a Fe-Mn-Si-Cr-Ni Alloy Coating. *Mater. Des.* **2020**, *193*, 108824. [CrossRef]
142. Li, C.; Xu, Y.; Jia, T.; Zhao, J.; Han, X. Numerical Simulation Research on Multifield Coupling Evolution Mechanism of IN625 Laser Cladding on Nodular Cast Iron. *Int. J. Adv. Manuf. Technol.* **2022**, *119*, 5647–5669. [CrossRef]
143. Qiao, X.; Xia, T.; Chen, P. Numerical Research on Effect of Overlap Ratio on Thermal-Stress Behaviors of the High-Speed Laser Cladding Coating*. *Chin. Phys. B* **2021**, *30*, 018104. [CrossRef]
144. Li, R.; Qiu, Y.; Zheng, Q.; Liu, B.; Chen, S.; Tian, Y. Finite Element Simulation of Temperature and Stress Field for Laser Cladded Nickel-Based Amorphous Composite Coatings. *Coatings* **2018**, *8*, 336. [CrossRef]
145. Krzyzanowski, M.; Bajda, S.; Liu, Y.; Triantaphyllou, A.; Mark Rainforth, W.; Glendenning, M. 3D Analysis of Thermal and Stress Evolution during Laser Cladding of Bioactive Glass Coatings. *J. Mech. Behav. Biomed. Mater.* **2016**, *59*, 404–417. [CrossRef]
146. Li, K.; Li, T.; Ma, M.; Wang, D.; Deng, W.; Lu, H. Laser Cladding State Recognition and Crack Defect Diagnosis by Acoustic Emission Signal and Neural Network. *Opt. Laser Technol.* **2021**, *142*, 107161. [CrossRef]

147. Cen, L.; Du, W.; Gong, M.; Lu, Y.; Zhang, C.; Gao, M. Effect of High-Frequency Beam Oscillation on Microstructures and Cracks in Laser Cladding of Al-Cu-Mg Alloys. *Surf. Coat. Technol.* **2022**, *447*, 128852. [CrossRef]
148. Yang, H.; Tang, Z.; Wan, L.; Wei, Q.; Wu, J.; Wang, A.; Jin, X.; Li, X.; Wu, Y.; Lu, G.; et al. Achieving Crack-Free CuCrZr/AlSi7Mg Interface by Infrared-Blue Hybrid Laser Cladding with Low Power Infrared Laser. *J. Alloys Compd.* **2023**, *931*, 167572. [CrossRef]
149. Zhang, P.; Chu, J.; Qu, G.; Wang, D. Numerical Simulation of Convex Shape Beam Spot on Stress Field of Plasma-Sprayed MCrAlY Coating during Laser Cladding Process. *Int. J. Adv. Manuf. Technol.* **2022**, *118*, 207–217. [CrossRef]
150. Feng, Y.; Pang, X.; Feng, Y.; Li, Z. Ultrahigh Hardness Coating with Excellent Crack Resistance Achieved by Ultrafine Eutectic. *Metall. Mater. Trans. A* **2022**, *53*, 2325–2330. [CrossRef]
151. Wang, Z.; Tan, M.; Wang, J.; Zeng, J.; Zhao, F.; Xiao, X.; Xu, S.; Liu, B.; Gong, L.; Sui, Q.; et al. Core-Shell Structural Iron Based Metal Matrix Composite Powder for Laser Cladding. *J. Alloys Compd.* **2021**, *878*, 160127. [CrossRef]